1.22 Constraints on Seismic Models from Other Disciplines – Constraints from Mineral Physics on Seismological Models

L. Stixrude, University of Michigan, Ann Arbor, MI, USA

R. Jeanloz, University of California at Berkeley, Berkeley, CA, USA

1.22.1 Introduction

Earth is unique among the planets as the only body for which we have a detailed picture of its internal structure. We may compare that part of seismology concerned with Earth structure to an experimental science concerned with a single, very large sample. The source of illumination is generated naturally, in the form of earthquakes, many each year large enough to generate measurable ground accelerations at the antipodes. (There are typically more than 10 major (magnitude 7–8), 100 large (magnitude 6–7), and 1000 damaging (magnitude 5–6) earthquakes each year. Prior to the current international moratorium, nuclear explosions have also provided seismic illumination of the Earth's deep interior: magnitudes of 5, 6, and 7 correspond roughly to yields of 32 kiloton, 1 megaton, and 32 megaton.) The detectors are seismic recording stations, which now number in the hundreds of the highest quality. The basic measurement is of the traveltime from source to receiver, from which can be deduced the elastic-wave velocity along the path of propagation; the displacement versus time (waveform) shown by the seismic record also provides information about the spatial gradients of wave velocity at depth. Millions of crossing rays have illuminated every corner of the interior, leading to models of Earth structure in which the velocity is considered known to within 1%. In addition, the frequencies of Earth's resonances (free oscillations or normal modes) excited by large earthquakes, typically determined to a part in 10^3 for hundreds of overtones, provide important information on the distribution of density at depth.

Such extraordinary precision rivals or exceeds our ability to measure elastic-wave velocities in the laboratory at conditions representative of most of the Earth's interior. In reality, the seismological determination of velocity is somewhat more limited than this comparison would suggest, primarily by spatial resolution: the smaller the region of interest, the larger the uncertainties.

Earth is unusual as an experimental sample in ways other than its large size. Pressure, temperature, and composition are all inhomogeneous, and the spatial variations of these quantities are due to

processes internal to the planet, rather than being externally imposed. Temperature and compositional fields both show large radial and lateral variations that are the product of Earth's origin, evolution, and dynamics. But how to determine these quantities? We have no *in situ* measurements of either temperature or composition below the crust, and seismology alone does not suffice: only the elastic-wave velocities and density are measured, not temperature or composition.

A central concern of mineral physics has been to uncover the nature of Earth's internal temperature and composition, with a view toward placing critical observational constraints on the planet's history and geological processes. For example, by recognizing the connection between the bulk sound velocity determined seismologically and the compressibility ($1/K_S$), Adams and Williamson showed that much of Earth's structure can be explained by an adiabatic variation of temperature with depth. (Two kinds of sound waves propagate through solids, compressional and shear (also referred to as longitudinal and transverse) that have velocities $V_P = \sqrt{[(K_S + \mu)/\rho]}$ and $V_S = \sqrt{(\mu/\rho)}$, respectively, with K being the adiabatic bulk modulus (or incompressibility), μ the shear modulus (or rigidity), and ρ the density. The bulk sound velocity, $V_B = \sqrt{(V_P^2 - 4/3 V_S^2)} = \sqrt{(K_S/\rho)}$, ignores the effects of rigidity and treats the material as a fluid.) By comparing seismological models and experimental – mostly shock-wave – data, Birch identified iron as the primary constituent of Earth's core, and the mean atomic mass of the mantle as being similar to that of certain xenoliths (rock fragments of the Earth's interior brought to the surface by volcanic processes). Ringwood, Akimoto, and others showed that seismologically observed mantle discontinuities can be explained by phase transformations observed in experiments on samples of mantle-like composition. In each case, a key to our current view of the Earth's origins and current vigorously convecting state were established.

It may seem at first surprising that materials of such different sizes, from thousand-kilometer structures in Earth to laboratory samples as small as a few microns – a range of 12 orders of magnitude – may be compared at all. (Though they are usually ignored for bulk samples, if one takes surface effects into account, the comparison can be extended down to the nanometer scale.) Actually, the basic approach is not unique to geophysics and forms the basis for understanding the structure and evolution of giant planets or stars. The theoretical basis

for spanning the range of length scales from atoms to planets lies at the heart of thermodynamics and statistical mechanics: the prediction that the equilibrium properties of materials should not depend on the size of the sample. There are deep connections to seismology as well: the analysis of the normal modes of vibration of an atomic lattice leads to concepts of dispersion and elastic-wave velocity that can be linked directly to analogous seismological problems. Relating the large to the small is essential for uncovering the temperature and composition throughout the Earth's interior. High-pressure devices and theoretical simulations figuratively transport us to the inaccessible interior, giving us a unique window into its nature.

From the point of view of materials theory, Earth is a particularly challenging object because it consists of solids and fluids (condensed matter) at moderate to high pressures. Unlike the gases that make up planetary atmospheres, the temperature-dependent constitutive relations between stress, strain, and strain rate (pressure, density, and deformation rate for a fluid) cannot be written down analytically. Much of the effort in mineral physics is devoted to discovering these constitutive relations, either by experimental measurement or by quantum mechanical theory.

The solid state is also complex in that elements organize themselves into multiple phases of different composition and crystal structure (i.e., geometric arrangement by which the atoms are packed together to form the crystal). Each phase has distinctive physical and chemical properties, and its behavior must be understood separately and in combination with other phases. The exploration of high pressure continues to be one of the frontiers of mineral physics, including the challenge of measuring physical properties in the laboratory at conditions of Earth's interior, and the ongoing discovery of new solid phases.

Perhaps the most challenging aspect of the solidity of materials making up the mantle is that it imposes limitations on our ability to scale from laboratory to Earth. These limitations arise from the heterogeneity inherent even in the purest sample in the form of grain boundaries and the differences in size, shape, and orientation of the constituent grains. So, for example, it is not possible to uniquely compute the seismic velocity of a rock from the properties of its constituent single crystals, although rigorous bounds can be formulated if the grains are randomly oriented. An exact computation would require

complete specification of the grain geometry. Although usually not the case for Earth materials, the bounds can be far apart in the presence of significant mechanical heterogeneities such as partial melts or cracks. More generally, some physical properties such as attenuation and scattering depend essentially on length scale, and often in ways that are difficult to predict.

The significance of the length scale of heterogeneity is intimately linked to the timescale of deformation. All materials contain defects, such as dislocations, interstitial atoms, and vacancies. When deformed at very high ('infinite') frequency, the types and concentrations of defects are of little consequence and the material deforms elastically because the defects are frozen in place. Seismic waves have much longer periods of deformation however – roughly 14 orders of magnitude greater than those of atomic vibrations. At these timescales, defects can move in response to deformation, leading to anelastic behavior with absorption of mechanical energy and lowering of the elastic wave relative to the elastic limit. In the limit of much longer periods of deformation, such as those that characterize mantle convection, the deformation is entirely viscous and dominated by the motion of defects.

The nature and degree of anelasticity depends in detail on defect types (point defects, dislocation, grain boundary), concentrations, and mobilities. Anelasticity is thus not a state function, in the usual thermodynamic sense, and can depend on the past history of the sample. This presents severe challenges to experimental control and characterization, and to our ability to relate the results to the Earth where the deformation history that the materials have undergone may be very different from those prepared in the laboratory. On the other hand, the fact that anelasticity depends on so many more variables than the elastic-wave velocity presents the opportunity for further characterizing the nature of Earth's interior in ways that are not possible through analysis of the elastic limit alone.

We will explore the relationship between minerals properties and Earth structure in more depth. Our approach will be that of the forward problem. We begin with the fundamentals of mineral elasticity, including the basic theory of lattice vibrations, dispersion and normal modes, and its relationship to the various experimental probes of elasticity, to the thermodynamic properties of minerals, and to the underlying quantum mechanics of bonding. Discussion of the elasticity of rocks includes an outline of the theory of composites as applied to the elastic constants, and the essentials of anelasticity. Finally, we consider the issue of scaling in length and timescale from the laboratory to the Earth. We end with thoughts on the prospects for the inverse problem; that is, formally inverting seismological observations for quantities such as the temperature and compositional fields at depth via knowledge of materials properties.

1.22.2   Mineral Elasticity

1.22.2.1   Overview

In the limit of ideal crystals and small deformations, the elasticity of solids is most usefully viewed in the context of the vibrational modes of crystalline structures. The theory of the dynamics of perfect crystals is our most powerful way of envisioning length scaling. It gives us a formally exact means of relating the elastic-wave velocity of samples ranging in size from submicron to in principle infinite size, limited only by considerations of surface effects at small scales and of self-gravitation as we approach planetary size. The material can be treated as a continuum at large scales, and its properties derived from consideration of the forces acting between atoms, that is, from a description at the smallest of scales. In particular, the seismic-wave velocities of a perfect crystal are determined by its crystal structure and the interatomic forces.

This approach of lattice dynamics is also important in geophysics because it underlies our understanding of the influence of temperature on physical properties, including thermal expansion that drives convection of the mantle and core, and seismic-wave velocities that provide images of our planet's interior. The theory of thermal conductivity also derives from concepts of phonons, which are the modes of oscillation of atoms in a crystal (analogous to the normal modes of the Earth). The theory of lattice dynamics is well developed, and there are many excellent texts covering the subject more deeply than we can here (Ashcroft and Mermin, 1976; Born and Huang, 1954; Dove, 1993). In addition to illustrating the connection between microscopic and macroscopic properties, our goals are to illustrate the relationship between experimental and geophysical measurements of elastic-wave velocities.

1.22.2.2   One-Dimensional Lattice Dynamics and the Continuum Limit

A good illustration of these concepts is provided by the normal modes of vibration of a linear chain of identical atoms of mass m separated by a distance a and connected with Hookean springs, for which the relationship between force F and displacement u is $F = Ku$, where K is the force constant (**Figure 1**). The potential energy is a quadratic function of the displacement of the atoms, and the equations of motion (force equals mass times acceleration, expressing conservation of linear momentum) are

$$m\frac{\partial u_n^2}{\partial t^2} = K\left[(u_{n+1} - u_n)^2 + (u_{n-1} - u_n)^2\right] \quad [1]$$

Here, u_n is the displacement of the nth atom from its ideal lattice site, located at the position na. Substituting a traveling-wave solution for u_n as a function of position and time $u = A\exp[i(\omega t - kx)]$, we find the dispersion relation (**Figure 1**):

$$\omega = 2\sqrt{\frac{K}{m}}\left|\sin\left(\frac{ka}{2}\right)\right| \quad [2]$$

where ω is the frequency (in rad s^{-1}), $k = 2\pi/\lambda$ is the wave number (in rad m^{-1}) (in two and three dimensions (2-D and 3-D), the wave vector specifies the

propagation direction and its magnitude gives the wave number), and λ is the wavelength (in meter/cycle) of the normal mode of vibration. The phase velocity describing the propagation speed of a given wavelength is given by $V_\phi = \omega/k$, whereas the group velocity that describes the propagation speed of a wave packet (i.e., many different wavelengths, and hence the wave energy) is $V_G = \partial\omega/\partial k$. In general, the linear monatomic chain is thus dispersive, with wavelength-dependent velocities and specifically $V_G < V_\phi$ (i.e., a low-pass filter: longer waves travel faster than shorter waves).

At long wavelength, as $k \to 0$, the group and phase velocities are the same (which means there is no dispersion, i.e., spreading out of a wave packet):

$$V = a\sqrt{\frac{K}{m}} = \sqrt{\frac{M}{\rho}} \quad [3]$$

where the last equality emphasizes the relationship with the seismic-wave velocity expressed in terms of an elastic modulus, $M = K/a$, and a density, $\rho = m/a^3$. Here, M is the longitudinal modulus, since propagation and polarization are parallel for the present 1-D example. The motion described by eqns [2] and [3], with $\omega \to 0$ as $k \to 0$, is referred to as an acoustic mode.
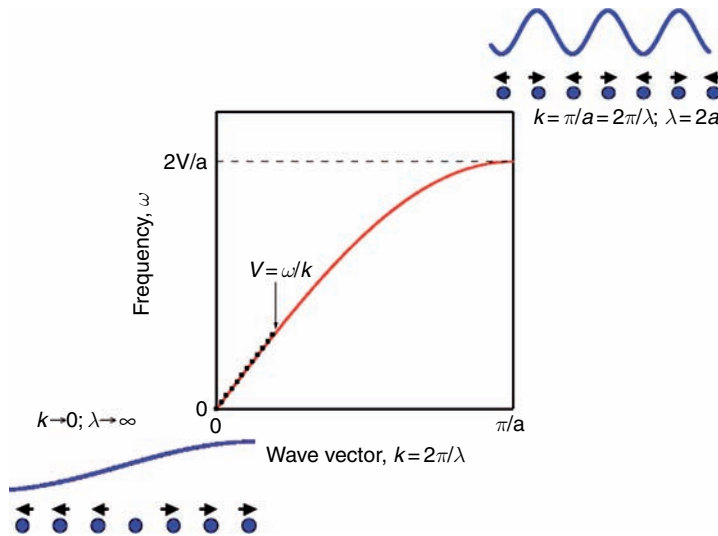
Figure 1   Phonon dispersion relation for the one-dimensional lattice (red line) indicating the relationship to the acoustic velocity as the slope at the origin (dashed black line). Schematically illustrated are vibrational modes, with arrows and blue curves indicating the sense of displacement of the atoms (blue circles) in the limits of long wavelengths (lower left) and of the shortest wavelengths (upper right). The group velocity (slope of the ω–k curve) vanishes at the Brillouin-zone edge, $k = \pi/a$, because shorter wavelengths cannot be propagated across the discrete row of atoms; consequently, there is a standing wave with no wave-energy propagation for $\lambda = 2a$.

Equation [3] applies to the continuum limit, with wavelengths being much larger than interatomic spacings, as is the case for seismic waves. Indeed, it agrees with our intuitive notions about seismic-wave velocities. As we increase the strength of the interatomic forces the velocity increases, as it would, for example, in the case of increasing pressure. Also, as we increase the mass of the atoms, the velocity decreases, as it would, for example, in the case of iron enrichment.

What do the normal modes look like in the limit of the wavelength approaching twice the interatomic spacing, $k \to \pi/a$? This is of interest because shorter wavelengths cannot be supported by the chain of discrete atoms (this limitation is identical to the Nyquist theorem encountered in Fourier and signal theory, which specifies that at least two samples per wavelength are needed to characterize a wave); in fact, normal modes with wavelengths less than twice the interatomic spacing are indistinguishable from those within the wave number range $k = 0$ to π/a. This range of wave numbers, defining the first Brillouin zone in reciprocal (wave number) space, contains complete information on all the normal modes that the chain of atoms can experience. At the Brillouin zone edge ($k = \pi/a$), the motion of each atom opposes its neighbors (**Figure 1**). Each bond is stretched or compressed by the same amount, producing the maximum frequency $\omega = 2\sqrt{(K/m)} = 2V/a$.

The particulate nature of matter thus produces velocity dispersion as wavelengths approach atomic (or unit-cell) dimensions, well below the continuum range. This is reflected in the nonlinear form of eqn [2] and, for example, the difference between the Brillouin-zone edge frequency and the linear extrapolation of eqn [2] to the Brillouin-zone edge $\omega = \pi V/a$. This type of dispersion is negligible in the usual geophysical context, and, for ideal crystals, scaling from laboratory samples to geophysical length scales is essentially exact. From eqn [2], we find that even for length scales corresponding to very small grains (1 μm), the dispersion is only about 1 part in 3000. This unity of length scales is modified by heterogeneity (e.g., grain boundaries) and anelasticity in real (nonideal) samples.

1.22.2.3   Experimental Methods

Experimental probes of the elastic-wave velocities have characteristic wavelengths that, while orders of magnitude smaller than those of seismic waves, lie well within the continuum, infinite-size limit of ideal crystals. Brillouin spectroscopy is most closely connected to the phonon spectrum (Duffy *et al.*, 1995; Jackson *et al.*, 2000; Sinogeikin and Bass, 2000; Weidner *et al.*, 1982). Here, one measures the normal-mode frequency of the acoustic branch at a small but finite value of the wave number related to the wavelength of the (generally visible) light used to probe the sample, with the ratio of frequency to wave number yielding the elastic-wave velocity. (The wave number is given by the magnitude of the scattering vector (i.e., the projection of the light's wavelength onto the direction of acoustic-wave propagation in the crystal) through a formula analogous to Bragg's law for X-ray diffraction. The frequency is observed as a Doppler-like shift of the scattered relative to the incoming light, and Brillouin spectroscopy can be thought of as the acoustic-mode analog of Raman spectroscopy, the latter scattering off the optic modes to be described below.) In impulsive stimulated scattering, a time-domain version of Brillouin spectroscopy, a phonon is excited by one laser and scatters light from a second laser, yielding information on elasticity, as well as thermal conductivity (Abramson *et al.*, 1999; Brown *et al.*, 1989; Zaug *et al.*, 1993).

Similarly, resonant ultrasound spectroscopy and ultrasonic interferometry determine the normal-mode frequencies of a macroscopic crystal (megahertz for typical experimental sample sizes), and are thus analogous to normal-mode studies of the Earth (Anderson and Isaak, 1995; Goto *et al.*, 1976; Jackson and Niesler, 1982). Other ultrasonic methods are analogous to body-wave seismology: an acoustic pulse of frequency in the range of mega- to gigahertz is generated via a transducer and the traveltime across the sample measured; multiple reflections and interference are used to maximize precision (Rigden *et al.*, 1991; Spetzler, 1970; Yoneda, 1990). High frequencies are essential so that the acoustic wavelength (10 μm$-$1 mm) is much smaller than the size of the sample ($\sim$1 mm for *in situ* high-pressure measurements).

All of these methods involve small ('infinitesimal')-amplitude waves. In addition, two classes of finite-compression methods are available: dynamic (shock wave) and static. In the first, a large-amplitude deformation wave is generated by impact of a projectile or a laser pulse into the sample, which is then compressed on a timescale of nanoseconds. The velocity of the resulting shock wave is then approximately equal to the longitudinal-wave velocity at low pressures (below the dynamic yielding point) and to the

bulk sound velocity at higher pressures (thermal and other corrections can be made to obtain more exact results). Above the dynamic yielding point, the shock front moves at close to the high-pressure bulk-sound velocity (i.e., fluid-like response), but rarefaction waves – inevitably generated at all free surfaces of the sample – propagate into the shock-loaded state at the isentropic sound velocity: this is measurable, with the initial decompression traveling at the longitudinal- (compressional-) wave velocity. The bulk sound velocity (V_B) and longitudinal-wave velocity (V_P) can thus be probed dynamically, and the shear-wave velocity (V_S) is obtained from the relation (Brown and McQueen, 1986; Duffy and Ahrens, 1992),

$$\frac{4}{3} V_S^2 = V_P^2 - V_B^2 \qquad [4]$$

The bulk sound velocity can also be determined in static experiments (Jeanloz and Thompson, 1983; Stixrude *et al.*, 1992). Using a diamond-anvil cell or another high-pressure device, one measures the volume (or density ρ) as a function of pressure via very slow (minutes–days) stepwise compression: X-ray diffraction is used to determine the compression, for example. The slope of the relationship yields the isothermal bulk modulus K_T, which is related to V_B through

$$V_B = \sqrt{\frac{K_S}{\rho}} \qquad [5]$$

and the correction from isothermal to adiabatic (K_S) bulk moduli which is small at room temperature.

One of the most important conclusions to arise from these various probes of material elasticity is that frequency dependence is essentially undetectable over 8 orders of magnitude: the shear- and longitudinal-wave velocities are indistinguishable from 100 THz (Brillouin) to 1 MHz (ultrasonic), and the bulk sound velocity is invariant from 100 THz to the essentially zero-frequency (DC) measurements of static compression. In contrast, the Earth shows measurable frequency dependence of the velocity over a much narrower range of lower frequencies (few hertz to millihertz) (Dziewonski and Anderson, 1981). The comparison with laboratory studies confirms the expectation that the magnitude of attenuation and the resulting dispersion increase with decreasing frequency.

1.22.2.4   3-D Lattice Dynamics: Polarization and Anisotropy

Only longitudinal elastic modes are possible in 1-D: shear elastic modes are higher-dimensional phenomena since the polarization (direction of atomic displacement) differs from that of propagation (wave vector). In 3-D, there are three acoustic branches, one corresponding to the P wave and two to the S waves (**Figure 2**: the optic modes are discussed below). All solids support both longitudinal and shear waves. In the case of isotropic solids (glasses) and liquids (just as at low enough deformation rates solids flow plastically, at high enough frequencies fluids transmit shear waves over finite distances), the two shear branches are degenerate. For nonisotropic media (crystals and liquid crystals), the two shear branches are in general distinct, although they may be degenerate along certain high-symmetry directions.

Anisotropy is the variation of the elastic-wave velocity with propagation polarization direction, and is governed by the fourth-rank elastic-constant tensor, c_{ijkl} (Kosevich *et al.*, 1986; Wallace, 1972). The polarizations and original slopes of the three acoustic branches for wave vector k are given by the Christoffel equation,

$$\rho V^2 = c_{ijkl} \hat{w}_i \hat{k}_j \hat{w}_k \hat{k}_l \qquad [6]$$

where w_i is the polarization vector, the carets indicate unit vectors, and we have used the Einstein notation (summation over repeated subscripts, and each subscript takes on each of its values, $i = 1, 2, 3$ (e.g., x, y, z directions)). The symmetry of the elastic-constant tensor reflects that of the point group of the crystal (Nye, 1985). For an isotropic solid (glass), there are only two independent elastic constants, which may be taken as the bulk and shear modulus. For cubic crystals, there are three, c_{11}, c_{12}, and c_{44}, referred to as longitudinal, off-diagonal, and shear, respectively; and as many as 21 for the lowest-symmetry point group (triclinic crystals). Evaluating eqn [6] for pure P-wave propagation ($k = w$) in cubic symmetry,

$$\frac{\rho V_P^2}{c_{11}} = 1 + 2A(k_1^2 k_2^2 + k_1^2 k_3^2 + k_2^2 k_3^2) \qquad [7]$$

where the anisotropy factor,

$$A = \frac{2c_{44} - (c_{11} - c_{12})}{c_{11}} \qquad [8]$$

completely determines the P-wave anisotropy (Karki *et al.*, 1997b). We have used the Voigt contraction for
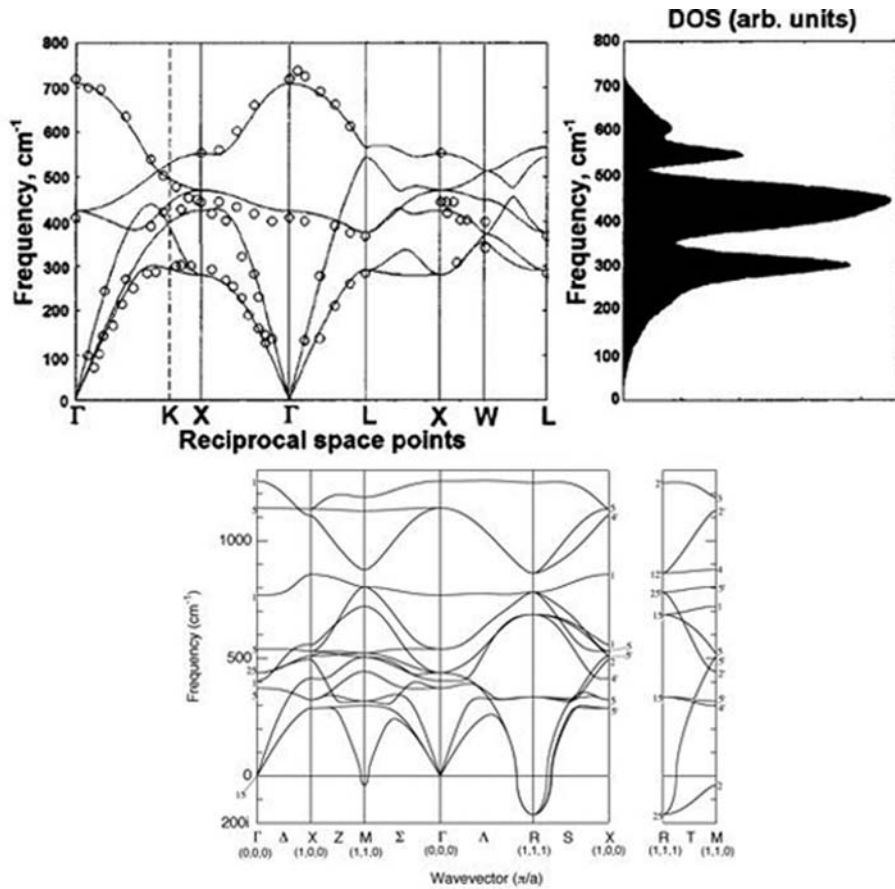
Figure 2   (Top) Phonon dispersion curves of periclase (MgO) according to density functional theory (lines) and experiment (circles), showing the three acoustic modes with zero frequency at the Brillouin-zone center (Γ point) and the three optic modes with finite frequency at Γ. On the right is the vibrational spectrum or density of states, $g(\omega)$, computed from the theoretical phonon dispersion curves: at each frequency, the total number of normal modes is indicated for all wave vectors intersecting the dispersion curves (this means that a higher density of modes is obtained from those portions of the curves having small group velocities, or vanishing $\partial\omega/\partial k$; also, due to the effects of 3-D, the number of modes contributing from each branch increases as $\sim k^2$, even without dispersion). (Bottom) Phonon dispersion curves of CaSiO$_3$ perovskite according to density functional theory, with unstable modes (shown as negative frequencies) at the M- and R-points and along the line from M–R. These unstable modes formed the basis for predicting a phase transformation in CaSiO$_3$ perovskite (Stixrude *et al.*, 1996) that has recently been confirmed experimentally. The meaning of the symbols identifying special points in reciprocal space are defined in terms of the wave vector, and are the same in the upper and lower figures. (Top) From Oganov AR, Gillan MJ, and Price GD (2003) *Ab initio* lattice dynamics and structural stability of MgO. *Journal of Chemical Physics* 118: 10174–10182. (Bottom) From Stixrude L, Cohen RE, Yu R, and Krakauer H (1996) Prediction of phase transition in CaSiO$_3$ perovskite and implications for lower mantle structure. *American Mineralogist* 81: 1293–1296.

the indices of the elastic constants: $11 \rightarrow 1$, $22 \rightarrow 2$, $33 \rightarrow 3$, $12 \rightarrow 6$, $13 \rightarrow 5$, $23 \rightarrow 4$. One can show that A also determines the azimuthal and polarization shear anisotropy. The right-hand side of eqn [7] gives $1 + 2/3A$, $1 + 1/2A$, and 1 for propagation along [111], [110], and [100], respectively.

We can evaluate the likely magnitude of single-crystal anisotropy if we assume that the interatomic forces are central and between nearest neighbors only, and we neglect coupling between strain and

vibrational modes. The elastic-constant tensor is then (Gieske and Barsch, 1968)

$$c_{ijkl} = (K - P)\frac{9}{z}\sum_{\alpha=1}^{z} \hat{r}_i^\alpha \hat{r}_j^\alpha \hat{r}_k^\alpha \hat{r}_l^\alpha \qquad [9]$$

where P is pressure, z the coordination number, and $\hat{r}^\alpha$ the unit vector between an atom and its nearest neighbor α; the sum is over all nearest neighbors. For body-centered cubic (b.c.c.) and face-centered cubic (f.c.c.) crystal structures, eqn [9] yields positive
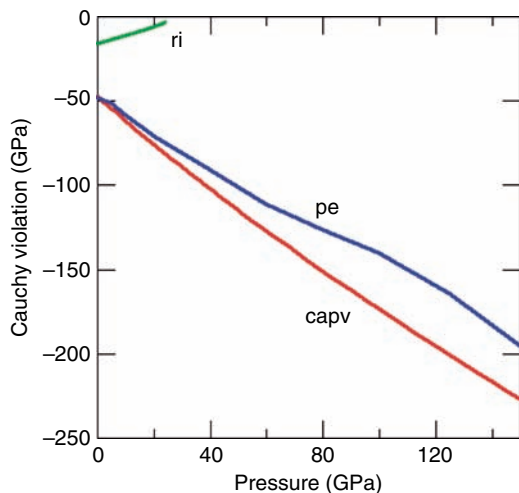
values of *A*, and therefore greater velocities along [111] and [110] than along [100]. The magnitude of the anisotropy is large: for f.c.c., $A = 1/2$, yielding peak-to-peak variations in the P-wave velocity of 30%. This simple model has been applied to oxides based on the argument that the elasticity is primarily governed by the oxygen sublattice and oxygen–oxygen repulsion, with the cations playing a passive, charge-balancing role.

The relative importance of central versus other interatomic forces can be deduced by comparing the elements of the elastic-constant tensor to the predictions of the Cauchy relations, which apply for purely central forces (**Figure 3**). (Angle-dependent and three-body forces are examples of such noncentral interactions between atoms. Weiner (1983) shows more generally that for centrosymmetric crystals the harmonic elastic moduli satisfy the Cauchy relations if the electron charge density follows the (homogeneous) deformation of the underlying lattice of nuclei.) For example, in a cubic material, the Cauchy relations predict

$$c_{12} - c_{44} = 2P \qquad [10]$$

In the case of MgO, often considered to be a prototypical ionic solid for which one would expect central forces to be dominant, eqn [10] is increasingly violated with increasing pressure (Isaak *et al.*, 1990; Karki *et al.*, 1997b). This shows that the interatomic forces become increasingly noncentral with increasing pressure, as expected on systematic grounds. One consequence of this change in forces is that the sign of the anisotropy changes with increasing pressure (**Figure 4**). Whereas at low pressure, *A* is large and positive, in accord with expectations based on eqn [9] and the f.c.c. oxygen
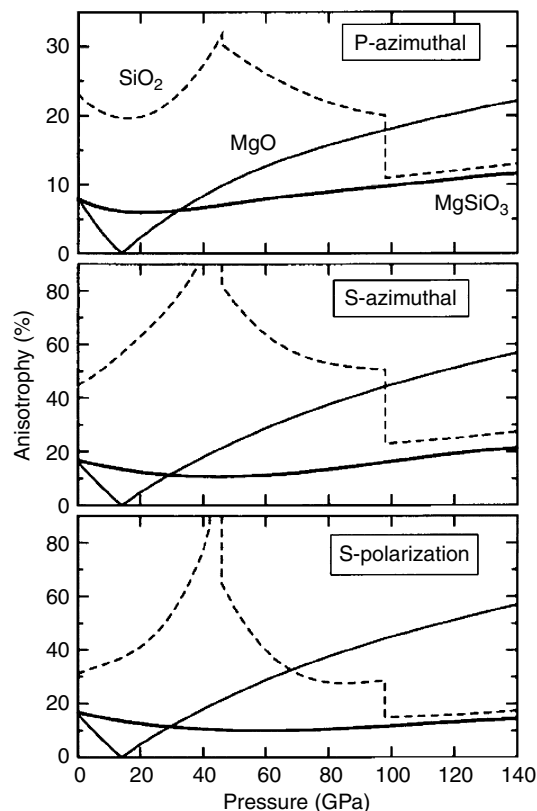
Figure 4 Elastic anisotropy of SiO_2 (dashed curves), MgO periclase (light solid), and $MgSiO_3$ perovskite (bold solid) according to density functional theory. P- and S-azimuthal anisotropy are the differences between the maximum and minimum P- and S-wave velocities, respectively, over all propagation and polarization directions, and the polarization anisotropy is the maximum difference in velocity between the two S-wave polarizations over all propagation directions. The discontinuous changes in the curve for SiO_2 are due to phase transformations from stishovite to the $CaCl_2$ structure at 47 GPa and to the α-PbO_2 structure at 100 GPa. Breaks in slope in the MgO and $MgSiO_3$ curves represent pressures at which the pattern of anisotropy changes. In the case of MgO, the break in slope coincides with a vanishing of the anisotropy that is due to a change in sign of the anisotropy factor *A* (eqn [8]). From Stixrude L (1998) Elastic constants and anisotropy of $MgSiO_3$ perovskite, periclase, and SiO_2 at high pressure. In: Gurnis M, Wysession M, Knittle E, and Buffet B (eds.) *The Core–Mantle Boundary Region*, pp. 83–96. Washington, DC: American Geophysical Union.

Figure 3 Violation of the Cauchy relation (eqn [10]) of three cubic minerals according to density functional theory: spinel-structured Mg_2SiO_4, ringwoodite (ri); NaCl-stuctured MgO, periclase (pe); and perovskite-structured $CaSiO_3$ (capv) (Karki and Crain, 1998; Karki *et al.*, 1997b; Kiefer *et al.*, 1997).

sublattice of MgO, at high pressure A becomes negative, with a magnitude at the core–mantle boundary greater than that at ambient pressure. The change in sign of A corresponds to a change in the fastest and slowest directions: [111] is fastest for P-wave propagation at ambient pressure, whereas [100] is fastest at the core–mantle boundary. Other minerals also show strong pressure dependence of the magnitude and sense of the anisotropy (Karki *et al.*, 2001).

Considerations of mechanical stability place constraints on the relative magnitude of the elastic constants of any material, whether single crystals or rocks. For isotropic symmetry, the stability condition is simply that the bulk and shear moduli be positive definite. For cubic symmetry, the conditions are

$$c_{44} > 0, \; c_{11} > |c_{12}|, \; c_{11} + 2c_{12} > 0 \qquad [11]$$

and for hexagonal symmetry,

$$c_{44} > 0, \; c_{11} > |c_{12}|, \; (c_{11} + c_{12})c_{33} > 2c_{13}^2 \qquad [12]$$

The more general statement from which stability conditions for arbitrary symmetry are derived is that the principal minors of the elastic-constant matrix (Voigt notation) must be positive definite (Nye, 1985). Elastic instabilities place fundamental constraints on the phases that exist in the Earth. For example, it has been argued that the predicted elastic instability in the b.c.c. phase of iron means that this phase cannot exist in the inner core, with important implications for the origin of anisotropy in this region (Stixrude *et al.*, 1994).

One of the most fundamental conclusions from experimental and theoretical studies of minerals is that the elastic anisotropy is much larger than that observed seismologically in most parts of the Earth. Peak-to-peak azimuthal variation in velocities of 10% or more are typical in mantle and core minerals, as compared with a few percent in the Earth. The single-crystalline anisotropy of some minerals is sufficiently large to produce cusps in the group velocity envelope (Helbig, 1984) (**Figure 5**). Experimental measurement and prediction of the single-crystal anisotropy is essential because it forms the basis for estimating the anisotropy of rocks, and places an upper bound on the rock anisotropy that can be produced by lattice preferred orientation. Most of the experimental methods discussed previously are capable of measuring the full elastic-constant tensor, and therefore the velocity in all directions. These measurements must be made on single crystals. In the case of Brillouin or ultrasonic interferometry, several measurements are necessary, varying the direction of the impulse with respect to the crystallographic axes in order to sample different directions in reciprocal space.

What is the origin of anisotropy in the mantle and core? There are at least two possible explanations, shape-preferred orientation and lattice-preferred orientation. These two mechanisms for generating anisotropy in a polycrystalline aggregate arise in principle from very different sets of processes, and so carry important implications for our understanding of mantle dynamics and evolution. In the case of lattice-preferred orientation, anisotropy
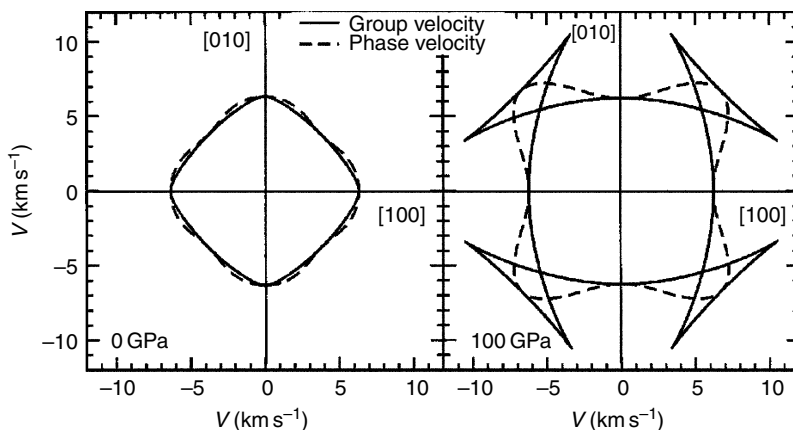
Figure 5   Group velocity (solid curves) and phase velocity (dashed curves) surfaces of *S* waves in MgO in the (001) plane at two pressures. The two velocities are close to each other at zero pressure due to relatively weak anisotropy, but they differ substantially at 100 GPa due to relatively strong anisotropy. From Karki BB, Stixrude L, and Wentzcovitch RM (2001) High-pressure elastic properties of major materials of Earth's mantle from first principles. *Reviews of Geophysics* 39: 507–534.

originates in the elastic anisotropy of the constituent crystals and is in general present for single- as well as multiphase aggregates. Since the single-crystal anisotropy can be large, it is natural to consider lattice-preferred orientation as the primary explanation in many cases (**Figure 4**). Knowledge of the single-crystal elastic anisotropy is not sufficient to determine that of a polycrystalline aggregate, however. For this, one must also know the texture, that is, the orientations of all the crystals in the aggregate.

Shape-preferred orientation arises from an inhomogeneous distribution of phases with different elastic properties. Anisotropy due to shape-preferred orientation scales with the contrast in physical properties between the phases, and therefore applies only to multiphase aggregates (composites). It can be large, for example, in cracked or partially molten rock. In the limit of large scales, variations of rock types (lithological variations) can induce anisotropy that affects seismic waves.

Presumably, both shape- and lattice-preferred orientation cause seismic anisotropy within the Earth. That the observed anisotropy is quantitatively much smaller than could be expected based on laboratory and theoretical studies of individual minerals and mineral aggregates strongly suggests that the seismological information is severely aliased. That is, the seismic wavelengths ($\sim 10^3$–10^6 m) are typically so much longer than the dimensions of crystals or even lithological variations, that they reflect only a broad spatial average of the true heterogeneity and anisotropy at depth.

1.22.2.5 Nontrivial Crystal Structures, Optic Modes, and Thermodynamics

Lattice vibrations are geophysically significant not only for their connection to elasticity, but also because they govern most thermodymamic properties of Earth materials, including the temperature dependence of the elastic constants. Most of the temperature dependence of the energy of a crystal comes from the increasing amplitude of atomic vibrations with increasing temperature. The derivation of the internal energy due to lattice vibrations is outlined in the texts listed above. Here we seek an intuitive understanding, simply quoting the result for the internal energy associated with atomic vibrations

$$U_{\mathrm{vib}} = \frac{1}{2}\sum_i \hbar\omega_i + k_{\mathrm{B}}T \sum_i \frac{\hbar\omega_i/k_{\mathrm{B}}T}{e^{\hbar\omega_i/k_{\mathrm{B}}T} - 1} \qquad [13]$$

where $\hbar$ is Planck's constant divided by 2π, k_{B} is Boltzmann's constant, and the sums are over all $3N$ vibrational modes with N being the number of atoms in the crystal. The first term is due to zero-point motion. The second term is the product of the energy of a particular vibrational mode ($\hbar\omega$) and the probability of excitation ('occupation') of that mode. The probability of occupation may appear unfamiliar because it is derived from the appropriate quantum (Bose–Einstein) statistics, but it does reduce to the Boltzmann factor $\exp(-\hbar\omega/kT)$ in the limit of high temperatures. The probability of occupation says that while very-high-frequency modes (such as the stretching of the O–H bond) will barely be excited until one reaches mantle temperatures, the part of the acoustic branch near the Brillouin-zone origin (i.e., wavelengths much larger than the interatomic spacing) is already fully excited even at room temperature.

Eventually, all vibrational modes are fully excited and the second sum on the right-hand side approaches a constant, equal to the number of modes ($3N$). In this Dulong–Petit limit, the vibrational energy is linear in temperature, and the heat capacity at constant density approaches a constant value,

$$C_\rho = \left(\frac{\partial U_{\mathrm{vib}}}{\partial T}\right)_\rho \to 3Nk_{\mathrm{B}} \qquad [14]$$

or $1.188 \, \mathrm{J\,K^{-1}\,g^{-1}}$ for a mean atomic mass typical of the mantle ($21 \, \mathrm{g\,mol^{-1}}$). Vibrational frequencies of Earth materials are such that the Dulong–Petit limit is obeyed to within a few percent at typical subcrustal temperatures.

A practical difficulty in using eqn [13] is that all the vibrational frequencies must be known, which is rarely the case for mantle phases, particularly at high pressure. By reformulating as a sum over energies rather than states, we reestablish the connection with the analysis of phonon dispersion outlined above, and develop a useful starting point for approximating the sums. The vibrational energy can then be written as

$$U_{\mathrm{vib}} = k_{\mathrm{B}}T \int_0^\infty \left(\frac{1}{2} + \frac{1}{e^{\hbar\omega/k_b T} - 1}\right) \frac{\hbar\omega}{k_{\mathrm{B}}T} g(\omega)\mathrm{d}\omega \qquad [15]$$

where the vibrational density of states $g(\omega)$ (see **Figure 2**) is normalized such that

$$3N = \int_0^\infty g(\omega)\mathrm{d}\omega \qquad [16]$$

The power of this reformulation is illustrated by one of the simplest approximations for $g(\omega)$, due to Debye,

$$g(\omega) = 9N\omega^2 \left(\frac{\pi V}{a}\right)^{-3} \qquad [17]$$

This is derived by treating the material as a homogeneous continuum: that is, ignoring optic modes (described below) and approximating the acoustic phonon branch as linear with slope equal to the acoustic velocity (see eqn [3]: for this case without dispersion $\omega \propto k$, and because $g(\omega) \propto k^2$ in 3-D, it is proportional to ω^2 as in eqn [17]). The quantity in parentheses, the Debye frequency, is just the result of linearly extrapolating the acoustic branch to the Brillouin-zone edge and is obtained by ensuring that eqn [16] is satisfied. (Ensuring that only $3N$ normal modes (i.e., $3N$ degrees of freedom) are present for a crystal of N atoms in 3-D takes into account the atomic constituents of the medium. It was Debye's genius to realize that a self-inconsistent model of a homogeneous continuum with underlying atomic structure would lead to a physically sound result.) In 3-D, the velocity is replaced by an appropriate average over all directions and polarizations, and the bond length by the mean atomic spacing. The squared-frequency dependence arises from the assumptions that the density of vibrational states is uniform in reciprocal space and that the first Brillouin zone is a sphere. The Debye approximation captures much of the essential features of the heat capacity, including the observation that it vanishes at zero temperature as T^3 and approaches the Dulong–Petit limit at high temperature.

Simple approximations to the vibrational density of states, like the Debye approximation, do not explicitly account for the structural complexity characteristic of most Earth materials: in particular, that several different atoms are typically present in each unit cell of the crystal structure (e.g., Mg and O in MgO). What influence do these complexities have on the normal modes of vibration? The essential features are captured by a linear chain, but now with two different spring constants (see also Kieffer, 1979) (**Figure 6**). The broken symmetry doubles the unit cell (i.e., two atoms, one of each color in each unit cell vs one atom per unit cell in the monatomic linear chain), and halves the first Brillouin zone. The
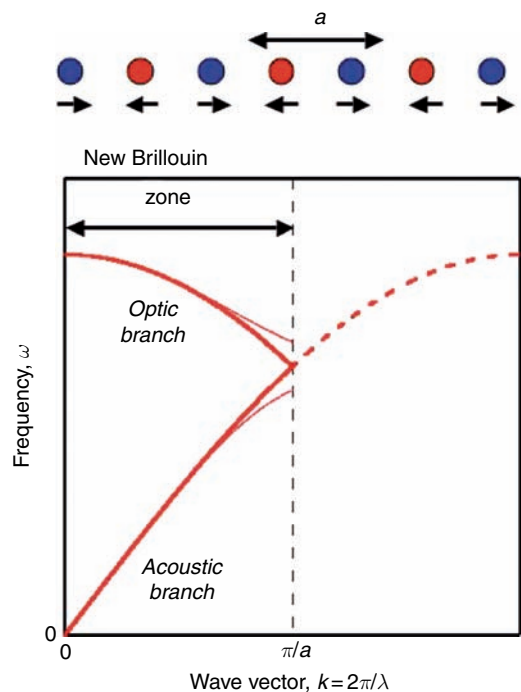
Figure 6   Phonon dispersion curve in a 1-D lattice with two types of atoms. The unit-cell dimension a is doubled compared with the monoatomic case, which halves the size of the Brillouin zone and folds the dispersion curve producing an optic branch. The pattern of vibration of the optic mode at zero wave vector is schematically illustrated; note that each unit cell has the identical pattern of vibration. The thin solid lines schematically illustrate the opening of an acoustic–optical gap that would be produced if the lattice contained two different force constants, or if the atoms had different masses.

relationship of the monatomic and diatomic unit cells in reciprocal space is one of folding the phonon branches so that the vibrational mode that appeared on the Brillouin-zone edge in the monatomic case is now folded back to the Brillouin-zone center. This is significant because now we have a vibrational mode of finite frequency at the Brillouin-zone center; as this can be observed with long-wavelength probes such as visible light, it is called an optic branch. In general, there are $3n$ mode frequencies at each wave number k in a 3-D crystal structure having n atoms per unit cell. (To be precise, we refer to the 'primitive' (smallest, irreducible) unit cell throughout this text. Other definitions of the crystallographic unit cell are often used for convenience.)

Now consider what happens when the difference in the two spring constants begins to grow or the masses of the two atoms in the unit cell are allowed

to differ (**Figure 6**). The frequencies of the two normal modes at the Brillouin-zone edge begin to separate, as is seen by considering the patterns of vibration. This zone-edge splitting appears whenever the material has bonds of different strength. So, for example, the contrast between the strong Si–O bond and the weaker inter-tetrahedral forces in quartz cause large zone-edge splittings, and a clear separation of acoustic and optic modes. Periclase, for which the contrast in bond strengths is much less, shows almost no acoustic–optic gap (in detail, non-nearest neighbor and noncentral forces open a gap even in periclase along certain high-symmetry directions; electron-polarization effects can also play an important role in shifting longitudinal-optic relative to transverse-optic modes).

In any case, at a given wave vector, we always have three acoustic modes and $3n - 3$ optic modes (n is the number of atoms in the unit cell). It is also known that longer-range interactions add structure to the $\omega-k$ dispersion relation: each successive coordination shell in a set of two-body interactions adds a Fourier component to the mode branch.

In the limit of no optical gap, the vibrational density of states may be reasonably approximated by the Debye relation (eqn [17]), regardless of how many atoms are in the unit cell, as the main modification of phonon dispersion is Brillouin-zone folding. This realization has led to the concept of Debye-like solids, periclase and corundum being prototypical examples (Anderson, 1995). Materials like quartz and those containing hydrogen bonds are typical counterexamples, for which more elaborate models such as those due to Kiefer are more appropriate (Kieffer, 1980). Even when deviations from a Debye-like spectrum are large, the influence on thermochemical properties is not necessarily significant, because these depend at high temperature only on low-order moments (weighted averages) of the vibrational density of states (Barron *et al.*, 1957) (**Figure 7**). Deviations are likely to be largest for water-rich hydrous phases, because the stretching frequency for the OH bond is so much larger than for any other bond thought to be important in the mantle (Williams, 1995). The essential relationship between acoustic and optic branches has also led to the idea of determining an average elastic-wave velocity from a measurement of the appropriate optic mode at the Brillouin-zone center (Merkel *et al.*, 2000).

Thermal expansion arises, in a first approximation, from the volume dependence of the vibrational frequencies (quasi-harmonic model). This modification

of the theory retains the normal-mode description of the frequencies, but allows the frequency spectrum to shift with compression. Anharmonicity generally refers to time dependence of the normal modes (e.g., due to mode mixing), and accounts for physical effects such as temperature dependence of the vibrational frequencies at constant volume that are not explained by quasi-harmonic theory (Gillet *et al.*, 1996)].

As the crystal compresses, bonds generally become stronger, the vibrational frequencies increase, and, from eqn [13], the vibrational energy decreases. The volume dependence of the vibrational energy produces a vibrational pressure that is positive and tends to expand the lattice. The vibrational or thermal pressure is

$$P_{\text{vib}} = \gamma \rho U_{\text{vib}} \qquad [18]$$

where the Grüneisen parameter is defined by

$$\gamma \equiv \frac{1}{\rho} \left(\frac{\partial P}{\partial U} \right)_{\rho} = \frac{\alpha K_T}{\rho C_{\rho}} = \left(\frac{\partial \ln T}{\partial \ln \rho} \right)_S \qquad [19]$$

and the second and third relations are thermodynamic identities. This makes explicit the relationship between thermal pressure and thermal expansivity α, and also shows that the Grüneisen parameter controls the magnitude of the adiabatic temperature gradient. For models of the vibrational density of states with a single characteristic frequency, such as the Debye or Einstein approximations, the following relation also holds,

$$\gamma = \frac{\partial \ln \omega}{\partial \ln \rho} \qquad [20]$$

establishing the link between quasi-harmonic thermal properties and the normal modes of the lattice. The Grüneisen parameter is dimensionless and empirically found to be about 1–3, so is a convenient way of capturing many related influences of temperature on the physical properties of minerals inside a planet (Mcqueen *et al.*, 1970; Stixrude and Lithgow-Bertelloni, 2005b; Wallace, 1972).

To introduce the influence of temperature on the elastic constants, consider the vibrational contribution to the bulk modulus. Taking the volume derivative of eqn [18], we see that the temperature dependence of the elastic constants will involve not only the Grüneisen parameter, but also its volume derivative

$$q = -\frac{\partial \ln \gamma}{\partial \ln \rho} \qquad [21]$$
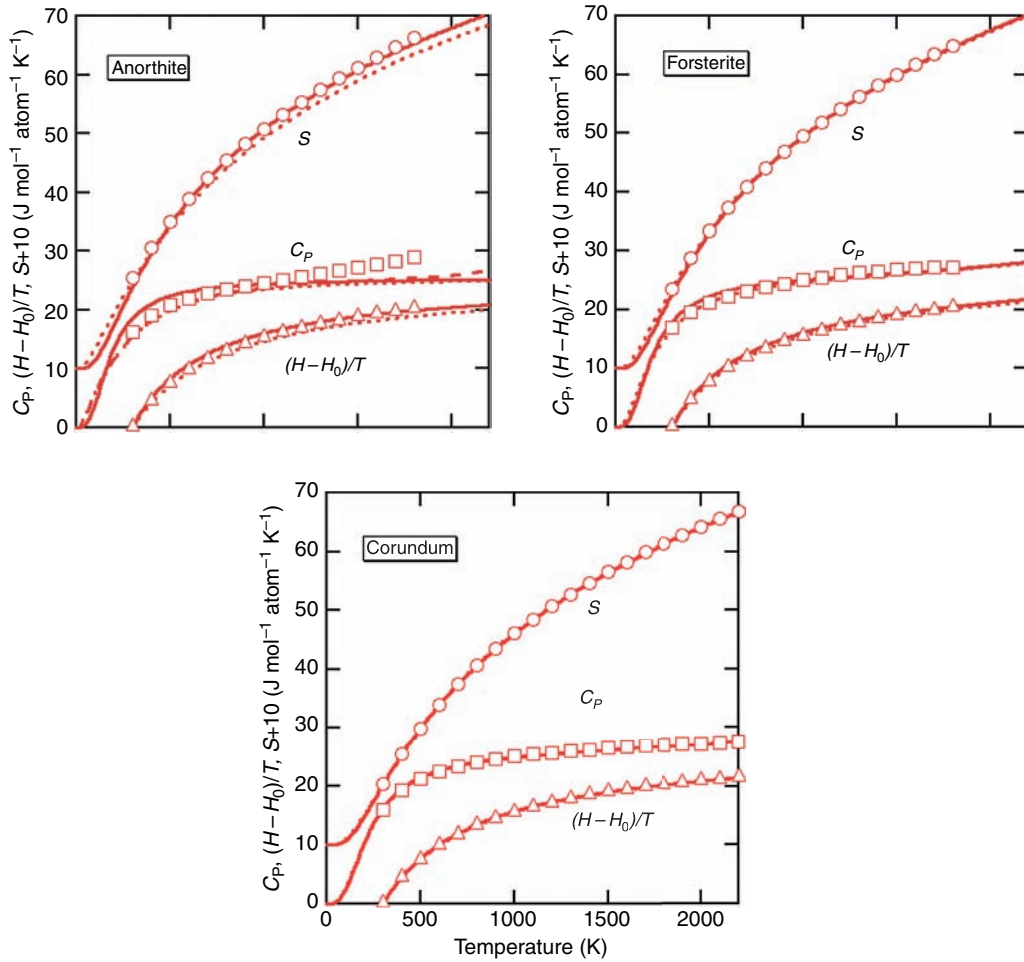
Figure 7 Experimentally derived (Robie and Hemingway, 1995) entropy (circles), heat capacity (squares), and enthalpy function (triangles) compared with (solid lines) Debye model with effective Debye temperature fit to the entropy at 1000 K, and (short dashed) the model of (Kieffer (1980)). For anorthite, the long dashed line shows the influence of cation disorder on the heat capacity according to the model of Holland and Powell (1998). The entropy is shifted upward for clarity. From Stixrude L and Lithgow-Bertelloni C (2005b) Thermodynamics of mantle minerals. I: Physical properties. *Geophysical Journal International* 162: 610–632.

where the parameter q is dimensionless and is thought to take on values in the range 1–3 for most mantle phases. The thermal pressure at temperatures above the Debye temperature can be approximated by

$$P_{TH} \approx 3nRT\gamma\rho \qquad [22]$$

and the thermal contribution to the adiabatic bulk modulus along an isochore is then just the volume derivative

$$K_{TH} \approx 3nRT(\gamma + 1 - q) \qquad [23]$$

An important consequence of the fact that $q > 1$ for most mantle materials is that the thermal pressure

and other thermal effects tend to decrease with compression. For example, the thermal expansivity and the influence of temperature on the elastic-wave velocities decrease with depth, with potentially important implications for mantle dynamics and the interpretation of seismic tomography (Chopelas and Boehler, 1989; Isaak *et al.*, 1992).

Because the Grüneisen parameter plays such a central role in our understanding of the thermal state of the Earth, there has been a great deal of interest in determining its dependence on compression. Many experimental data are consistent with the assumption that q is constant without necessarily requiring it. More recent experimental analyses

and theoretical studies suggest that q tends to decrease with compression (Agnon and Bukowinski, 1990; Speziale *et al.*, 2001), and analytical forms have been proposed (Stixrude and Lithgow-Bertelloni, 2005b).

1.22.2.6   Influence of Pressure and Temperature on the Elastic Constants

An important feature of the Earth is that compressions are large – the characteristic pressure is a large fraction of typical zero-pressure values of mineral bulk moduli – and the characteristic temperature is larger than typical vibrational energies of Earth materials. This means that measurements of the pressure and temperature derivatives of the elastic constants near ambient conditions do not suffice to give us a meaningful picture of the variation of these quantities over the conditions of Earth's interior. Indeed, experimental measurements show that the bulk modulus varies by more than a factor of 2 over the mantle pressure range. Such large changes are seen in the density and other properties too, and led Birch to apply the theory of Eulerian finite strain to understanding the Earth's interior. The theory of finite strain has been generalized to encompass the elastic constants (Davies, 1974), and has recently been reformulated in a thermodynamically self-consistent manner (Stixrude and Lithgow-Bertelloni, 2005b). Only the final results are discussed here.

The variation of the bulk and shear moduli with volume and temperature are, respectively,

$$
\begin{aligned}
K = {} & (1 + 2f)^{5/2} \\
& \times \left[K_0 + (3K_0 K_o' - 5K_0)f + \frac{27}{2}(K_0 K_0' - 4K_0)f^2 \right] \\
& + (\gamma + 1 - q)\gamma\rho\Delta U_{\text{vtb}} - \gamma^2\rho\Delta(C_V T)
\end{aligned}
\tag{24}
$$

$$
\begin{aligned}
G = {} & (1 + 2f)^{5/2} \left[G_0 + (3K_0 G_0' - 5G_0)f \right. \\
& \left. + \left(6K_0 G_0' - 24K_0 - 14G_0 + \frac{9}{2}K_0 K_0' \right)f^2 \right] \\
& - \eta_s\rho\Delta U_{\text{vib}}
\end{aligned}
\tag{25}
$$

where f is the Eulerian strain measure,

$$
f = \frac{1}{2}\left[\left(\frac{V}{V_0}\right)^{-2/3} - 1 \right]
\tag{26}
$$

and subscript '0' indicates the value of a quantity at the reference state (e.g., ambient conditions), primes

indicate pressure derivatives, and Δ indicates the difference between the temperature of interest and the temperature of the reference state. The quantity η_S takes on positive values near unity for mantle phases, and derives from the shear part of the fourth-rank tensor formed from the strain derivative of the tensorial generalization of γ, which we have assumed to be isotropic. Taking typical values of γ_0 and q (1 and 2, respectively), the temperature-dependent terms show that both moduli decrease with increasing temperature at constant volume. The decrease with increasing temperature at constant pressure is greater than that at constant volume according to

$$
\left(\frac{\partial M}{\partial T}\right)_P = \left(\frac{\partial M}{\partial T}\right)_V - \rho C_V\gamma M_0'
\tag{27}
$$

where M stands for either the bulk or shear modulus.

Finite-strain theory suggests systematic expressions for the values of the pressure derivatives of the elastic constants (Karki *et al.*, 2001; Stixrude and Lithgow-Bertelloni, 2005b). It has been known for some time that the Eulerian finite strain theory owes its success at least in part to that fact that it rapidly converges to experimentally measured equations of state with increasingly higher orders of the finite strain. In fact, for many materials, the lowest-order terms suffice. The term linear in f in the equation of state vanishes when $K_0' = 4$, a value that is typical of mantle phases and many other materials as well. We may take the same approach in the case of eqns [24] and [25], and ask what relationships are implied by the vanishing of the term linear in f within the square brackets. In the case of the shear modulus, this yields a relationship between the pressure derivative of G and the ratio of shear modulus to bulk modulus, which is satisfied approximately for mantle phases. The pressure derivative of the shear modulus thus appears to scale with the value of the shear modulus itself.

We may relate the elastic moduli of mantle phases to those found seismologically via a compilation of experimental and theoretical results for the parameters appearing in eqns [24] and [25] (**Figure 8**). Comparison to seismological observations tends to support the standard model of a homogeneous peridotite composition that produces a series of phase transformations with increasing depth. (Peridotite is a rock primarily composed of the mineral olivine. Model mantle compositions, based on comparison
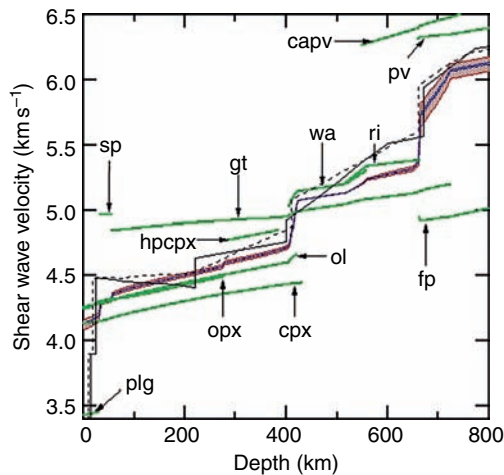
Figure 8   Computed shear-wave velocities of a model mantle composition (blue), and of the individual phases of the assemblage (green) along the 1600 K adiabat computed self-consistently with the phase equilibria and physical properties according to the method of Stixrude and Lithgow-Bertelloni (2005a). The Voigt–Reuss (red) and Hashin–Shtrikman (blue) bounds on the aggregate velocity are shown. Thin black lines are radial seismological models: (solid) PREM (Dziewonski and Anderson, 1981); (dashed) AK135 (Kennett and Engdahl, 1991). Adapted from Stixrude L and Lithgow-Bertelloni C (2005b) Thermodynamics of mantle minerals. I: Physical properties. *Geophysical Journal International* 162: 610–632.

with seismology, the genesis of magmas, and analysis of mantle xenoliths typically contain 50–60% olivine, and lesser amounts of orthopyroxene, clinopyroxene, and garnet.) The velocity of the upper mantle is spanned by that of olivine, orthopyroxene, clinopyroxene, and garnet; in the shallow transition zone (410–520 km), by clinopyroxene, majorite, and wadsleyite; and in the deep transition zone (500–660 km), by Ca-perovskite, ringwoodite, and majorite. Velocities in the lower mantle are spanned by those of Mg-perovskite, magnesiowüstite, and Ca-perovskite. In the upper mantle and transition zone, we find that the change in shear-wave velocity due to phase transformations exceeds the influence of pressure on the velocity of any one phase. This suggests the essential role that phase transformations play in producing the anomalous velocity gradient of the transition zone, and emphasizes the importance of going beyond the elasticity of individual minerals in understanding mantle structure, as discussed further in the next section.

One of the most remarkable patterns in the temperature and compositional derivatives of the elastic
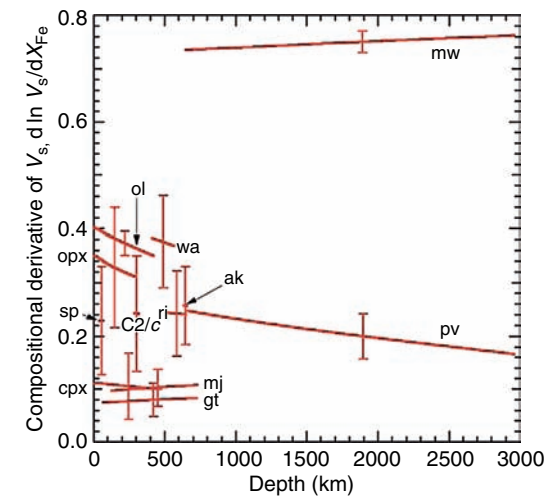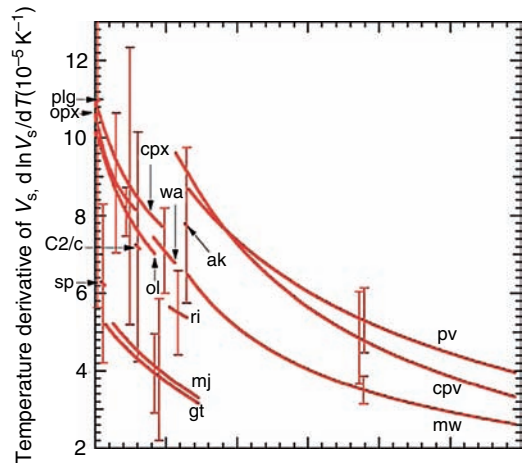
Figure 9   Variation of the shear-wave velocity with respect to (top) temperature and (bottom) composition. From Stixrude L and Lithgow-Bertelloni C (2005b) Thermodynamics of mantle minerals. I: Physical properties. *Geophysical Journal International* 162: 610–632.

moduli, aside from the large influence of compression discussed above, is the large difference between garnet-majorite and other phases (**Figure 9**). The compositional derivative for garnet and majorite (and clinopyroxene) is only a third of those of olivine and orthopyroxene, while the temperature derivatives of garnet and majorite are approximately half those of olivine and orthopyroxene. The contrast in compositional derivatives can be traced directly to the shear modulus of Mg- and Fe-end members of the phases: while the shear modulus of fayalite is 40% less than that of forsterite, that of almandine is actually slightly greater than that of pyrope, partially offsetting the effect of the greater density of almandine on V_S. The contrast in temperature derivatives

can be related to experimental measurements of dG/dT of the dominant species: 8 and 9 MPa K^{-1} for pyrope and majorite, respectively, compared to 15 MPa K^{-1} for forsterite. One consequence of the unusual properties of garnet is that the influence of temperature and iron content is sensitive to bulk composition. Specifically, more garnet-rich compositions, such as basalt, are less sensitive to variations in temperature or iron content than garnet-poor bulk compositions such as harzburgite (basalt is a rock primarily composed of pyroxene and plagioclase feldspar that makes up most of the oceanic crust and is produced by partial melting of the mantle, whereas harzburgite is a rock that is richer in olivine than the average mantle and is thought to be the residuum of partial melting of the mantle) (Speziale *et al.*, 2005a).

1.22.3 Rock Elasticity

1.22.3.1 Overview

Knowledge of mineral elasticity is necessary for estimating the elastic properties of a rock, but it is not sufficient. There are two primary considerations. The first is that rocks are heterogeneous. In the mantle, this heterogeneity is most pronounced at the grain scale (1–10 mm): every part of the mantle is made of several different mineral phases, each with different elastic properties. The difference in elastic properties between coexisting minerals is generally larger than that between different mantle rock types. The second difficulty is that minerals tend to be preferentially aligned by deformation. The alignment is neither perfect, in which case the elasticity would reduce to that of a single crystal, nor negligible. Indeed, the detection of preferential alignment via the resulting anisotropic propagation of seismic waves is one of our most powerful potential probes of mantle flow.

In principle, one needs to know – in addition to the elastic-constant tensors of the constituent minerals – the location, size, shape, and orientation of each mineral grain in the assemblage. However, such a detailed description is neither practical nor useful: a part of the Earth's mantle, the size of a typical mantle body wave (100 km), contains on the order of 10^{21} individual mineral grains, assuming 1 cm grains! This is another statement of the spatial aliasing problem described above. Model statistical distributions of mineral geometry play an important role, in particular in the analysis of preferred orientation.

Idealizations, in which either the preferred orientation or the spatial inhomogeneity, or both, are simplified, and permit exact solutions or rigorous bounds, are also important.

Additional complications arise at finite frequency: dissipative mechanisms exist in aggregates that are not present in single crystals, and these are thought to be important for producing attenuation and dispersion in the mantle, particularly at grain boundaries.

1.22.3.2 Composites Theory

Consider first a homogeneous isotropic medium, corresponding to a glass or a liquid. The elasticity is completely characterized by two elastic constants, which may be taken to be the bulk modulus, K, and shear modulus, G. The longitudinal- and shear-wave velocities for all propagation and polarization directions are

$$V_P = \sqrt{\frac{K + 4/3G}{\rho}} \quad V_S = \sqrt{\frac{G}{\rho}} \qquad [28]$$

where ρ is the density and, in the case of a liquid deformed on a timescale long compared with its Maxwell relaxation time, $G = 0$.

Consider an inhomogeneous system consisting of N isotropic phases with distinct elastic properties, such that phase α has bulk and shear moduli K^α and G^α and $\alpha = 1, \cdots, N$. Suppose that the only properties of the grain geometry we know are the volume fractions of the phases ϕ^α. The volume fraction is the only feature that is uniquely determined by the usual equilibrium thermodynamics, and is thus independent of the history of the sample. The stress and strain tensors are now functions of position

$$\sigma_{ij}(\mathbf{x}) = c_{ijkl}(\mathbf{x})\varepsilon_{kl}(\mathbf{x}) \qquad [29]$$

$$\varepsilon_{ij}(\mathbf{x}) = S_{ijkl}(\mathbf{x})\sigma_{kl}(\mathbf{x}) \qquad [30]$$

where the compliance tensor is the inverse of the elastic-constant tensor,

$$S_{ijkl} = c_{ijkl}^{-1} \qquad [31]$$

The volume average stress and strain of the rock is assumed related to that in each of the phases by

$$\bar{\sigma}_{ij} = \sum_\alpha \phi^\alpha \bar{\sigma}_{ij}^\alpha \qquad [32]$$

$$\bar{\varepsilon}_{ij} = \sum_\alpha \phi_\alpha \bar{\varepsilon}_{ij}^\alpha \qquad [33]$$

where the bars indicate volume averages. We define the effective elastic moduli of the composite as

$$\bar{\sigma}_{ij} = c^*_{ijkl} \bar{\varepsilon}_{kl} \qquad [34]$$

If we assume that the average stress and strain in each phase is a unique function of the average stress and strain, respectively, of the aggregate, then it is possible to show that the values of c^* are bounded such that

$$M^*_R = \left(\sum_{\alpha} \frac{\phi^{\alpha}}{M^{\alpha}} \right)^{-1} < M^* < \sum_{\alpha} \phi^{\alpha} M^{\alpha} = M^*_V \qquad [35]$$

where M refers to either K or G, and the bounds M^*_R and M^*_V correspond, respectively, to the assumption that the stress (Reuss bound) or strain (Voigt bound) are homogeneous throughout the composite (Hill, 1963; Watt *et al.*, 1976). Except in special geometries, neither of these approximations is correct: the assumption of constant stress requires the opening of gaps between grains, while the assumption of constant strain violates mechanical equilibrium. Indeed, the assumptions embedded in eqns [32] and [33] are in general not justifiable, and one of the complications of composites theory is that the stress tensor can no longer be treated as symmetric (e.g., Juanzemis, 1967).

Ignoring these complications, the Voigt and Reuss bounds limit the possible degree of anisotropy due to inhomogeneous arrangement of phases. This type of anisotropy is sometimes referred to as shape-preferred orientation. Plane layering is the classic example for which Voigt and Reuss bounds can be realized (Backus, 1962). The P-wave velocity for waves propagating normal to the layers is $\rho V^2_P = K_R + 4/3 G_R$, while that for propagation parallel to the layers is $\rho V^2_P = K_V + 4/3 G_V$. Thus, heterogeneity produces anisotropy. This relationship has been examined on the atomic level as well. There are several crystal structures in which layers of more compressible units, for example, Mg coordination polyhedra, alternate with layers of stiffer units such as Si polyhedra. Such alternation leads to the large anisotropy of the olivine structure (Hazen *et al.*, 1996; Wentzcovitch and Stixrude, 1997).

For illustration, we compare the Voigt and Reuss bounds of a typical mantle lithology (peridotite) in **Figure 10**. The bounds are wide in the shallow mantle due to the extremely low velocity of plagioclase, and in the vicinity of the 660 km discontinuity due to the much higher velocity of perovskite than garnet, whereas they are nearly coincident in the shallow transition zone where wadsleyite and garnet
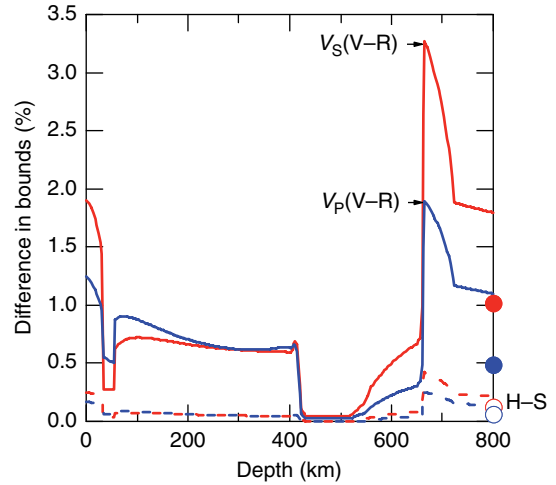
Figure 10   Differences between the Voigt and Reuss (solid) and Hashin–Shtrikman (dashed) bounds for P- (blue) and S- (red) wave velocities in a model mantle composition (Workman and Hart, 2005) along a self-consistent 1600 K adiabat. Symbols represent the values at the core–mantle boundary.

have similar velocities. In the lower mantle, the bounds differ by less than 2% and by less than 1% at the core–mantle boundary. These results suggest that shape-preferred orientation in subsolidus peridotites is unlikely to be the source of anisotropy in the D″ layer at the base of the mantle, as has previously been proposed on the basis of the contrast in elastic properties between perovskite and periclase (Karato, 1998).

It is not possible to estimate more precisely the value of the effective elastic moduli without further information. It is common in the literature to quote the so-called Voigt–Reuss–Hill (VRH) mean, which is simply the arithmetic mean of the Voigt and Reuss bounds (Hill, 1952). This value is not rigorously justified as a best estimate of the actual effective moduli.

With further assumptions about the distribution of the phases, it is possible to derive narrower bounds. The Hashin–Shtrikman analysis (Hashin and Shtrikman, 1963) assumes that the distribution of phases is statistically random and that the elastic properties of the aggregate are given as a solution to a variational problem. So, for example, regular arrangements such as layering are excluded. The Hashin–Shtrikman bounds, given in compact form by Berryman (1995), are narrower than the Voigt–Reuss bounds in most cases, including for the mantle (**Figure 10**). Watt *et al.* (1976) recommend that the Hashin–Shtrikman bounds should generally be used

in reporting the elastic properties of multiphase materials, rather than the Voigt–Reuss bounds, or the VRH average. However, this may be misleading since the Hashin–Shtrikman bounds are based on a limiting assumption that excludes geometries that are important in some parts of the Earth (e.g., layering).

In certain cases, the Voigt–Reuss and Hashin–Shtrikman bounds are too wide to yield useful estimates. This can occur when the moduli of the constituent phases differ significantly, as in the case of a porous solid or a partial melt. In such cases, the analysis of specific geometries may be useful. Typically, one assumes that one phase is the host (i.e., the solid rock) and the other is treated as an inclusion (air, water, or melt). Results for specific inclusion shapes have been derived, including spheres, needles, disks, and penny-shaped cracks (Berryman, 1995). For a given volume fraction of inclusions, the effective moduli are most similar to those of the host for spherical inclusions, whereas large aspect-ratio disks or cracks have the largest influence on the shear modulus (**Figure 11**). It should be noted that very little is known concerning the actual form of melt inclusions in partial melts within the mantle. The relevant controlling parameters are many, including the pressure, temperature, bulk composition and deformation history, and may be influenced by nonequilibrium effects.

An additional ambiguity in the computation of the effective elastic moduli of isotropic composites arises

from the intrinsic anisotropy of crystals. Even in the case of a monophase aggregate, the effective elastic moduli are inherently uncertain unless the texture has been completely specified (Watt et al., 1976). Hill (1952) showed that rigorous bounds correspond to the assumption of homogeneous strain and homogeneous stress, respectively. The Voigt (homogeneous-strain) bounds are

$$K_V^* = \frac{1}{3}(A + 2B) \qquad [36]$$

$$G_V^* = \frac{1}{5}(A - B + 3C) \qquad [37]$$

where A, B, and C, are, respectively, the mean diagonal, off-diagonal, and shear elastic constants:

$$A = \frac{1}{3}(c_{11} + c_{22} + c_{33})$$

$$B = \frac{1}{3}(c_{12} + c_{13} + c_{23}) \qquad [38]$$

$$C = \frac{1}{3}(c_{44} + c_{55} + c_{66})$$

The Reuss (homogeneous-stress) bounds are

$$K_R^* = \frac{1}{3(a + 2b)} \qquad [39]$$

$$G_R^* = \frac{5}{4a - 4b + 3c} \qquad [40]$$

where a, b, and c are similar to A, B, and C, but with the components of the compliance tensor replacing those of the elastic-constant tensor. The Hashin–Shtrikman bounds for the monophase aggregate are narrower (Hashin and Shtrikman, 1962). Expressions have been derived for cubic, tetragonal, orthorhombic, hexagonal, trigonal, and monoclinic Bravais lattices (Watt, 1988, and references therein). The difference between Voigt and Reuss bounds for the shear-wave velocity of olivine at ambient conditions is 2%. The difference tends to increase with increasing single-crystal anisotropy. For materials with very large anisotropy, such as periclase at the core–mantle boundary (azimuthal shear anisotropy = 60%), Voigt and Reuss bounds on the shear modulus differ by 30% and the Hashin–Shtrikman bounds differ by 5% (Karki et al., 2001). Spinel is an example of a mineral that is extremely anisotropic at ambient conditions, and for which bounds are wide (Yoneda, 1990).

Preferred orientation (preferential crystallographic alignment) of the constituent grains results in macroscopic anisotropy detectable by seismic
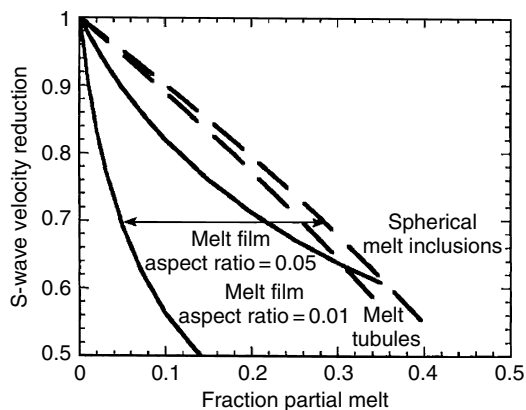
Figure 11 The ratio of the S-wave velocity of melt-bearing mantle to that of solid mantle for varying melt fractions and melt geometries. The arrow corresponds to the variation in melt fraction implied by the inferred P-wave velocity depression of 10% in the ultra-low-velocity zone at the base of the mantle. From Williams Q and Garnero EJ (1996) Seismic evidence for partial melt at the base of Earth's mantle. *Science* 273: 1528.

waves. The preferred orientation is characterized by the orientation distribution function,

$$f(\mathbf{g})d\mathbf{g} = \frac{dV_g}{V} \qquad [41]$$

where $\mathbf{g}$ is the rotation matrix that relates the crystallographic axes to the spatial or laboratory reference frame and dV_g/V is the volume fraction of crystals with orientation lying within the range $d\mathbf{g}$. The effective elastic moduli of the aggregate may then be estimated by (Bunge *et al.*, 2000)

$$c_{ijkl}^* = \int_g g_{im}g_{jn}g_{k0}g_{lp}c_{mnop}f(\mathbf{g})d\mathbf{g} \qquad [42]$$

where the effective elastic moduli are referred to the laboratory frame, and the elastic-constant tensor in the integrand is referred to the crystallographic frame. This expression yields the Voigt bound on the effective elastic moduli; the Reuss bound involves the compliances. Two simple cases of orientation distribution functions are of special interest (Stixrude, 1998). If the texture is perfect, that is, all crystals are identically aligned, then the effective elastic-constant tensor is identical to that of the single crystal rotated into the laboratory frame. Such a texture might be considered the asymptotic limit of lattice-preferred orientation produced by mantle flow. A transversely anisotropic aggregate is produced if deformation is dominated by an easy-glide plane. In this case, the effective elastic-constant tensor has hexagonal symmetry with the symmetry-axis normal to the glide plane.

1.22.3.3   Attenuation and Dispersion

When deformed by small stresses over short time-scales, the mantle behaves nearly elastically, propagating shear waves, whereas at long timescales it behaves like a fluid, deforming viscously in mantle convection. (Though not relevant to the immediate discussion, rock also behaves as a fluid under the short but high-amplitude stresses of impact-induced shock.) The boundary between these two types of behavior is characterized by the Maxwell relaxation time,

$$\tau_M = \frac{\eta}{G} \qquad [43]$$

where η is the viscosity. For the upper mantle, $\tau_M \sim 1000$ years is determined from glacial rebound.

At seismic periods, deformation is also not perfectly elastic. The relative amount of elastic energy

lost per cycle, dE/E, defines the quality factor Q, the inverse of which is referred to as the internal friction or attenuation

$$Q^{-1} = \frac{dE}{E} \qquad [44]$$

Attenuation entails dispersion. (This results from causality, the requirement that the mechanical energy of the wave cannot propagate faster than the signal velocity, as encapsulated by the fact that the frequency-dependent elastic modulus and attenuation are not independent: they are Hilbert transform-related real and imaginary components of the complex modulus, [47], and therefore satisfy integral conditions (Kramers–Kronig relations), e.g., Bracewell (1999).) The acoustic-wave velocity depends on the wavelength or frequency of the probe (**Figure 12**). This kind of dispersion – which involves nonequilibrium processes, with mechanical energy converted to heat – is distinct from the dispersion we encountered in the context of lattice dynamics of perfect crystals, which is an equilibrium phenomenon arising from the particulate nature of matter.

Simple models are useful for thinking about attenuation and dispersion even when they do not correspond to geophysically relevant materials. The Maxwell model is the simplest, consisting of an elastic spring and a dashpot in series. The Voigt model has these two elements in parallel. At short periods, both of these simple models produce elastic behavior
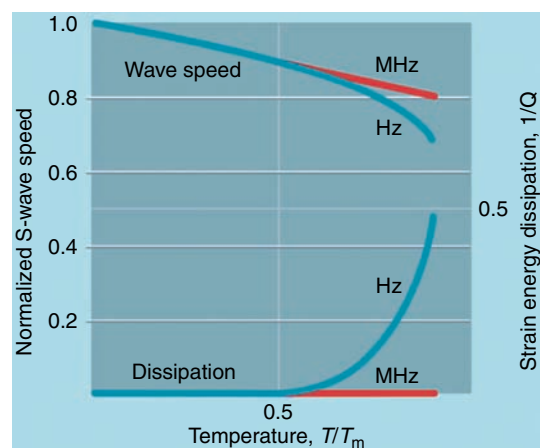
Figure 12   Schematic representation of the variation of acoustic-wave velocity (upper curves) and attenuation (Q^{-1}) (lower curves) with temperature at high frequencies (red) and lower frequencies within the seismic band (blue). From Jackson I (2000) Geophysics – Taking the Earth's temperature. *Nature* 406: 470–471.

governed by the spring. At long periods, the behavior is very different. Whereas the Maxwell model produces a purely viscous, unrecoverable response, governed by the dashpot, the Voigt model shows anelastic behavior: time dependent, but fully recoverable. The so-called Kelvin or standard linear solid consists of a Voigt model in series with a spring. The simplest model that shows the full range of response – elastic, anelastic, and viscous – is the Burgers model, which can be thought of as a Maxwell and Voigt solid in series. See, for example, Cooper (2002) for a recent discussion of these models.

These simple models make an important point. Viscous flow, which governs mantle convection, and anelastic deformation, which causes attenuation and dispersion in the seismic band, are considered as separate dashpots. While the connection to real materials is not obvious, it is likely that viscosity and attenuation are governed by separate microscopic deformation mechanisms if for no other reason than that the strain rates and total strains are so vastly different. Experimental measurements of viscosity, which are more numerous than measurements of seismic attenuation at relevant mantle conditions, are not necessarily a reliable guide to the dependence of attenuation on pressure, temperature, or composition.

Consider the response of these models to periodic loading,

$$\sigma = \sigma_0 e^{i\omega t} \tag{45}$$

which produces the strain response,

$$\varepsilon = \varepsilon_0 e^{i\omega t + \delta} \tag{46}$$

In most experiments, the attenuation is actually measured by the phase lag δ. The elastic modulus is complex and frequency dependent,
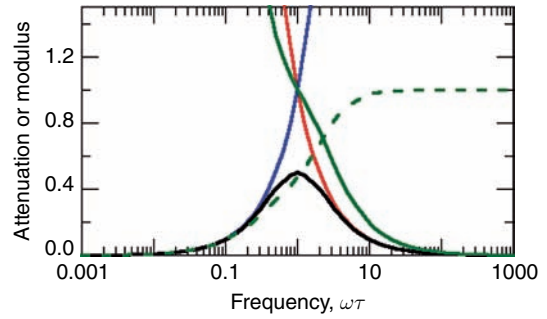
$$M(\omega) = M_R + iM_I \tag{47}$$

and the attenuation can also be written as the ratio of imaginary to real parts $Q^{-1} = M_I/M_R$. The acoustic-wave velocity is

$$V = \sqrt{\frac{M}{\rho}} \tag{48}$$

where ρ is the density.

The simple models described all predict attenuation that depends strongly on frequency (**Figure 13**). For the Maxwell solid, $Q^{-1} = 1/\omega\tau$, and for the Voigt solid, $Q^{-1} = \omega\tau$, where τ is the characteristic

Figure 13 Frequency dependence of the attenuation (solid curves) and modulus (dashed curve for the Burgers model) for simple mechanical models: Maxwell (red), Voigt (blue), Kelvin (black), and Burgers (green).

relaxation time. The standard linear solid shows Maxwell-like and Voigt-like behavior in the limit of zero and infinite frequency, respectively, with a peak attenuation centered at $\omega\tau = 1$:

$$Q^{-1} = \frac{\omega\tau}{1 + (\omega\tau)^2} \tag{49}$$

and the velocity dispersion is

$$V(\omega) = V(0)\left(1 + Q_{max}^{-1}\frac{(\omega\tau)^2}{1 + (\omega\tau)^2}\right) \tag{50}$$

For the Burgers model,

$$Q^{-1} = \frac{1 + 2\omega^2\tau^2}{2\omega\tau + \omega^3\tau^3} \tag{51}$$

there is a Maxwell-like decrease of attenuation with increasing frequency, interrupted by a region near $\omega\tau = 1$, where the dependence on frequency is much reduced. Depending on the details of how the Burgers model is parametrized, this shoulder may become a small peak.

Much of the literature on microscopic mechanisms of attenuation in solids has focused on the materials that show clear peaks in the attenuation spectrum. The dependence of the peak amplitude and frequency on temperature and material characteristics is essential for identifying the mechanism(s) responsible. Among the mechanisms that have been identified in this way are the migration of defects, the exchange of substituents in solid solution, dislocation motion, grain-boundary relaxation, and thermal currents (Jackson and Anderson, 1970; Nowick and Berry, 1972). Because so many mechanisms can contribute to the attenuation, it is often necessary to specially prepare the sample to have, for example,

high purity or uniform grain size, in order to produce a spectrum with a single clear peak. Many silicate liquids show attenuation that is well described by a single characteristic relaxation time (Rivers and Carmichael, 1987).

Perhaps the most important result from studies of mantle-like materials is the absence of attenuation peaks (Jackson *et al.*, 2002). Attenuation is found to vary slowly and monotonically with frequency over a broad spectrum. The reason for this behavior is not clear. It is possible that there exists a broad and nearly continuous spectrum of relaxation times. The behavior is similar to the so-called high-temperature background found in many materials (Nowick and Berry, 1972). Even those materials that show distinct peaks at low temperature may exhibit featureless attenuation spectra at high temperature.

In the case of attenuation dominated by elastically accommodated grain-boundary sliding, the featureless, nearly flat attenuation spectrum may be rationalized as follows (Jackson *et al.*, 2002). The characteristic relaxation time is

$$\tau_{gb} = \gamma \frac{\eta_{gb} d}{G\delta} \qquad [52]$$

where d is the grain size, δ is the width of the grain-boundary region, γ is of order 1, and η_{gb} is the grain-boundary viscosity (much less than the viscosity of the bulk). A spectrum of relaxation times might be produced by a distribution of grain sizes, grain-boundary widths, and grain-boundary viscosities. In particular, the effective grain-boundary viscosity could exhibit a wide range because of the variable presence of grain-boundary irregularities or impurities that would tend to inhibit sliding.

The following empirical expression represents the data of Jackson *et al.* (2002) within the seismic frequency band (~1–100 s periods) (**Figure 14**)

$$Q^{-1}(P,\ T,\ \omega) = Ad^{-m}\omega^{-\alpha}\exp\left(-\alpha\frac{E^* + PV^*}{RT}\right) \quad [53]$$

$$V(P,\ T,\ \omega) = V(P,\ T,\ \infty)\left[1 - \frac{1}{2}\cot\left(\frac{\alpha\pi}{2}\right)Q^{-1}(P,\ T,\ \omega)\right] \quad [54]$$

where ω is the frequency, d is the grain size, $m = 0.28$ is the grain size exponent, $\alpha = 0.26$ is the frequency exponent, $E^* = 430$ kJ mol^{-1} is the activation energy, V^* is the activation volume, and R is the gas constant. For the experimental value of α, the factor multiplying Q^{-1} in eqn [53] has the value 1.16. The
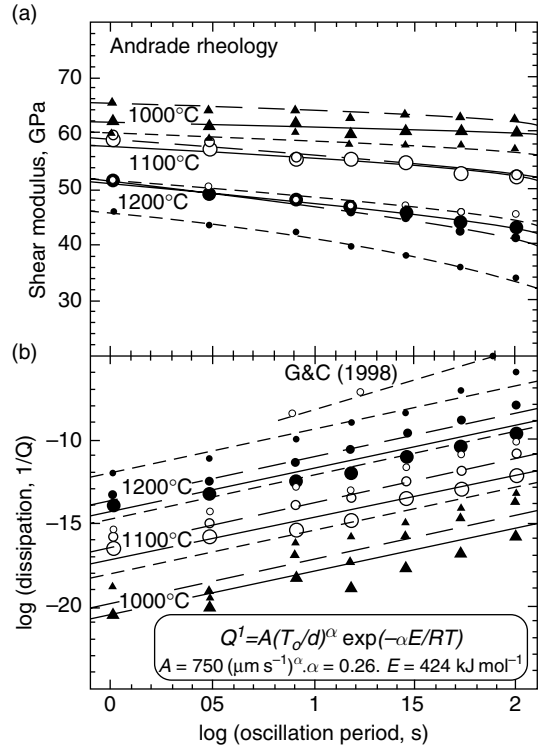
Figure 14 Grain-size sensitivity of the high-temperature mechanical behavior of olivine polycrystals. Data for specimens 6261, 6365, and 6381 of average grain size 23.4, 12.4, and 2.9 mm, are denoted by the large, medium, and small plotting symbols and by the solid, long-dashed, and short-dashed curves, respectively. Solid circles, open circles, and solid triangles denote data for 1200°C, 1100°C, and 1000°C CA6, respectively. (a) Shear modulus. Curves labeled with temperature indicate the modulus dispersion associated with Andrade models fitted simultaneously to $G(T_o)$ and $Q^{-1}(T_o)$ where $T_o = 2\pi/\omega$ is the oscillation period (cf. eqns [53] and [54]). (b) The log (dissipation). Lines represent the preferred fit (eqns [7] and [8]) to the entire 1000–1300 C, 1–100 s data set for all four specimens, except for the uppermost line representing the results of Gribb and Cooper (1998) for a resynthesized dunite of 2.8 mm grain size at 1200 C. From Jackson I, Fitzgerald JD, Faul UH, and Tan BH (2002) Grain-size-sensitive seismic wave attenuation in polycrystalline olivine. *Journal of Geophysical Research – Solid Earth* 107: N12.

activation volume is currently unconstrained, which means that the influence of pressure on attenuation is highly uncertain. The relationship between attenuation and dispersion is made explicit by eqn [54].

The experimental results can be compared with attenuation spectra proposed for the Earth. The absorption band model (Anderson and Given, 1982) consists of a broad frequency range over which Q^{-1} depends weakly on frequency, bounded by narrower

low- and high-frequency ranges where Q^{-1} decreases to zero. The intermediate-frequency range of this model, the absorption band, agrees well with experimental results. The estimates of the value of α based on seismological observations are consistent with those found experimentally at similar frequencies. But experimental support for the boundaries is lacking. At long periods, experiments show that the attenuation will continue to increase with increasing period and at a higher rate, with $\alpha = 1$ (Gribb and Cooper, 1998; Jackson *et al.*, 2002). At the high-frequency end, there is no indication of a sharp transition requiring a larger value of α. In fact, there is an indication in the data that the attenuation becomes less sensitive to frequency at high frequency (Cooper, 2002).

The influence of partial melt is generally to increase the attenuation (Faul *et al.*, 2004; Jackson *et al.*, 2004). The frequency dependence is also affected by partial melt. A broad absorption peak is superimposed on a high-temperature background. The origin of this peak appears not to be the melt squirt mechanism that has been widely discussed, but elastically accommodated grain-boundary sliding enhanced by partial melt. For probable mantle-grain sizes and attenuation in the seismic band, Q is nearly independent of frequency for 1% partial melt.

The influence of crystallographically bound hydrogen on the attenuation is currently not well constrained, although it is known that viscosity decreases with increasing hydrogen concentration (Mei and Kohlstedt, 2000a, 2000b).

The bulk attenuation – that is, time dependence of volume compression due to a change in hydrostatic pressure – has not been measured for mantle materials, and is generally assumed to be small. In the limit that bulk attenuation vanishes, the attenuation of longitudinal and shear waves is related by

$$Q_P^{-1} = \frac{4}{3}\left(\frac{V_S}{V_P}\right)^2 Q_S^{-1} \qquad [55]$$

For composites, however, because volume compression generally leads to local shear deformations being distributed throughout the medium, bulk attenuation can arise on the multigrain length scales relevant to seismology simply because of the presence of heterogeneous elastic properties and shear-dissipation mechanisms throughout the medium. Mechanisms that have been proposed for bulk attenuation thus include coupling to first-order phase transitions (Heinz *et al.*, 1982).

1.22.4 Seismological Elasticity and Anelasticity

1.22.4.1 Scaling

When the scale length of heterogeneity is comparable to the seismic wavelength, there are two additional considerations. The first is dispersion due to structure. This is seen in observations of surface waves, the velocity of which depend on frequency. This frequency dependence is mostly due to the fact that larger wavelengths sample greater depths where the intrinsic acoustic velocity is greater.

Random heterogeneity can produce scattering of seismic waves (Frankel and Clayton, 1986). Consider a random medium with average velocity *v*, characterized by heterogeneity of length scale *a* and velocity perturbation *d*, and probed by acoustic waves with wavelength λ. On average, the first-arriving waves tend to select paths that preferentially sample the high-velocity heterogeneities; in this sense, the medium appears to have a wave velocity slightly greater than *v*. In addition, the velocity depends on wavelength, that is, heterogeneity causes dispersion. The direct wave is attenuated, as energy is redirected due to scattering, but this is essentially different from the intrinsic attenuation discussed above for which mechanical energy is dissipated by being converted to heat. The difficulty, however, is that scattering due to heterogeneity has many of the same characteristics as intrinsic attenuation and dispersion of seismic waves, so the two causes of seismic-wave attenuation as a function of distance along the wave path are difficult, if not impossible, to disentangle. This means that any interpretation of attenuation in terms of the strong temperature dependence expected from intrinsic (dissipative) mechanisms, for example, needs to be treated with caution.

What is the scale of heterogeneity in the mantle? The magnitude of the heterogeneity is largest at the grain scale, with differences in shear-wave velocity between coexisting minerals being 10–30% throughout most of the mantle (except for the shallow transition zone) as well as near the core–mantle boundary (**Figure 15**). The ratio of the grain size typically observed in mantle xenoliths (1–10 mm) to teleseismic wavelengths is $d/\lambda \sim 10^{-7} \ll 1$ characteristic of Rayleigh scattering. In this long-wavelength limit, the apparent attenuation falls with increasing wavelength like $(d/\lambda)^3$ and is probably negligible as long as the heterogeneity is weak (say,
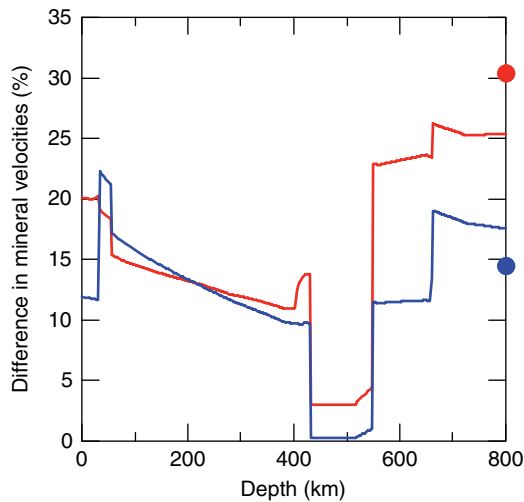
Figure 15   Maximum difference in the shear (red) and longitudinal (blue) velocities of coexisting phases in a model mantle composition. Symbols represent the values at the core–mantle boundary.

less than 1–10%). The grain-scale heterogeneity indicated in **Figure 15** can plausibly be accommodated within the Rayleigh-scattering model, but it is less likely that the stronger heterogeneity associated with partial melt or major compositional variations (e.g., mixtures of core metal and mantle silicates) can also be considered in this weak-scattering limit. Moreover, the grain size of the mantle is still highly uncertain at great depth, particularly below the zone of magma genesis.

Larger-scale heterogeneities, approaching or comparable to seismic wavelengths, are also likely in the mantle. At the mid-ocean ridge, basalt and a depleted residuum, harzburgite, are generated, both of which have significantly different physical properties from undifferentiated mantle. The initial scale length of heterogeneity may be taken as the thickness of the oceanic crust (~7 km), which is likely to scatter seismic waves significantly. The magnitude of the velocity difference depends on depth (**Figure 16**). Basalt is slower than peridotite at shallow depths, reflecting the well-known difference in velocity between crust and mantle. Basalt then becomes much faster near 100 km depth because of the transition to eclogite (plagioclase and pyroxenes forming garnet under pressure) that increases velocities by approximately 10%. Velocity contrasts in the lower mantle are not as well constrained, but appear to be less than 10%. For comparison, one seismological study found that scattering of P waves could be
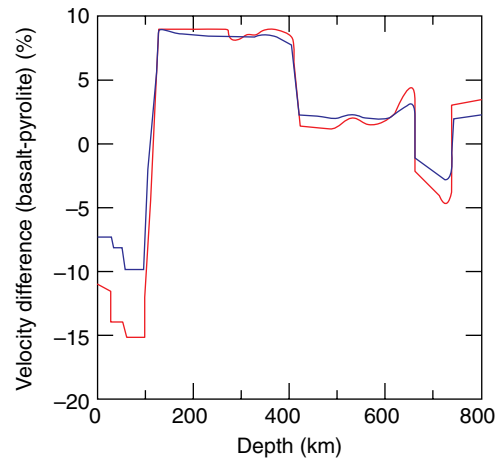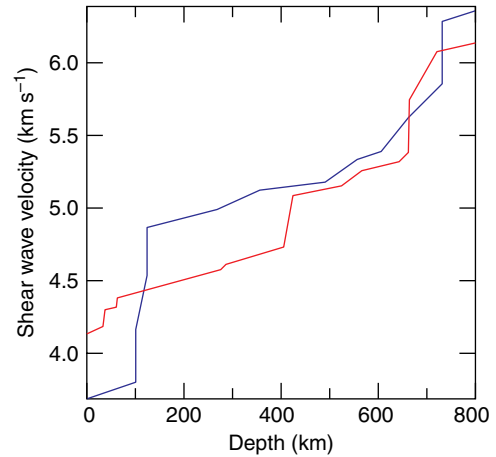
Figure 16   (Top) Velocity of basalt (blue) compared with that of a model mantle composition (red). (Bottom) the difference between the velocities of basalt and average mantle for shear (red) and longitudinal (blue) wave velocities.

explained by heterogeneity with scale length 8 km and magnitude 1% uniformly distributed throughout the mantle, but this result is probably strongly biased due to contamination from heterogeneity at the base of the mantle (Hedlin *et al.*, 1997).

1.22.4.2   Uncertainties

The largest source of uncertainty in constructing isotropic models of radial upper-mantle and transition-zone structure is the elastic constants of minerals at high pressure and temperature (**Table 1**). The propagated uncertainty in the elastic shear-wave velocity is approximately 1.3% or 0.06 km s^{-1} (Stixrude and Lithgow-Bertelloni, 2005a). This is somewhat larger than the difference between Voigt

Table 1   Elastic properties of major mantle phases

Phase	K_0	dK_0/dX	K_0'	$-dK/dT$	G_0	dG/dX	G_0'	$-dG/dT$
plg	84(5)	-	4.0(10)	4(1)	40(3)	-	*1.1*(5)	6(3)
sp	197(1)	12(2)	5.7(2)	29(3)	109(10)	−24(16)	0.4(5)	13(2)
ol	128(2)	7(2)	4.2(2)	18(1)	82(2)	−31(2)	1.4(1)	14(1)
wa	169(3)	*0*(13)	4.3(2)	22(6)	112(2)	−40(12)	1.4(2)	18(1)
ri	183(2)	16(7)	4.1(2)	23(2)	120(2)	−25(10)	1.3(1)	17(2)
opx	107(2)	−7(4)	7.0(4)	19(5)	77(1)	−25(5)	1.6(1)	13(2)
cpx	112(5)	7(6)	5.2(18)	18(9)	67(2)	−6(2)	*1.4*(5)	*11*(4)
hcpcx	121(1)	*0*(10)	5.5(3)	20(3)	90(1)	−19(10)	1.5(1)	17(2)
capv	236(4)	-	3.9(2)	22(13)	165(12)*	-	2.5(5)*	26(4)
ak	211(4)	*0*(10)	4.5(5)	*20*(6)	132(8)	*25*(12)	1.6(5)*	*21*(4)
gt	170(2) − 9Y	7(3)	4.1(3) + 0.1Y	16(2)	94(2)	4(3)	1.3(2) + 0.1Y	10(1) − 2Y
st	314(8)	-	4.4(2)	31(18)	220(12)	-	*1.6*(5)	*36*(5)
pv	251(3)	30(40)*	4.1(1)	23(4)	175(2)	−37(40)*	1.7(2)*	25(3)*
fp	161(3)	18(3)	3.9(2)	21(1)	130(3)	−83(3)	2.2(1)	26(1)

Symbols and Units: K, adiabatic bulk modulus (GPa); G, shear modulus (GPa), X, Fe/(Mg + Fe); $Y, mj/(py + mj)$; subscript o indicates values at zero pressure, primes indicate pressure derivatives; dK/dT and dG/dT in $MPa K^{-1}$. Italicized entries are unconstrained by experiment. Asterisk indicates values taken from density functional theory calculations. After Stixrude and Lithgow-Bertelloni (2005b) and references therein.

and Reuss bounds throughout most of this region, and considerably more than the difference between the Hashin–Shtrikman bounds (**Figure 10**). Uncertainties in computed elastic properties arise mainly because of the need to extrapolate existing measurements taken over limited ranges of pressure and/or temperature to mantle conditions. For a few phases, large discrepancies exist in measured properties that cannot be reconciled at present. An important example is garnet-majorite, for which Brillouin spectroscopy yields a value for $G' = 1.3(2)$ (Sinogeikin and Bass, 2002), while ultrasonic studies yield a much higher value of 1.9 (Liu *et al.*, 2000). We have followed the discussion of Jiang *et al.* (2004) in favoring the Brillouin value in this case, but must emphasize that (as in other instances of apparent discrepancy) there may be real differences between samples (as yet not recognized, let alone controlled for) and that it is not necessarily a question of poor measurements.

In addition to these uncertainties, many important properties remain to be measured at all. For example, the shear modulus of clinopyroxene and akimotoite at elevated pressure are currently estimated on the basis of systematic relations, or density functional theory calculations.

Another kind of uncertainty comes from the linkage between velocity dispersion and attenuation, because there is virtually no constraint on the latter at mantle conditions based on laboratory experiments. Simple models, based on the Weertman law

or a constant activation volume, apparently do not reproduce the qualitative features of seismological radial Q models (Faul and Jackson, 2005). While attenuation has a small effect on the velocity, the velocity variation of tomographic models is also small, so that intrinsic dispersion is a large part of the 3-D structure (Karato, 1993). Progress will come from experimental measurements of Q^{-1} in the seismic band at elevated pressure, an enormous challenge.

In the lower mantle, the reliability with which seismological observations can be interpreted is probably limited by our understanding of the relevant mineral-scale physics. For example, the recently discovered high-spin–low-spin transition (Badro *et al.*, 2003, 2004; Pasternak *et al.*, 1997) appears to have a significant, but still uncertain influence on the density and elasticity (Lin *et al.*, 2005; Speziale *et al.*, 2005b). It also remains to be understood at what pressure, or over what pressure range, this transition occurs in the lower mantle, and how this range depends on temperature, iron content, and other compositional variables. Valence transitions induced by pressure, for example, between ferric and ferrous iron, also remain poorly understood (Frost *et al.*, 2004), as does the phase diagram of the third most abundant lower-mantle constituent, calcium silicate perovskite. A temperature-induced transition from a low-temperature tetragonal phase to a high-temperature cubic phase has been predicted (Stixrude *et al.*, 1996), and low-temperature structural distortions

have been seen experimentally (Shim *et al.*, 2002), but the details remain uncertain. This transition should be accompanied by a large elastic anomaly (15% in shear-wave velocity).

Constructing mineralogical models of anisotropic structure remains a considerable challenge. There has been substantial progress from experiment and theory in our knowledge of the full elastic-constant tensors of major mantle minerals (Karki *et al.*, 2001). We still have a great deal to learn about deformation mechanisms, and in particular dominant slip planes at mantle conditions and at relevant strains and strain rates. Experimental results now exist for many mantle minerals (Cordier, 2002). For lower-mantle minerals, it is important to keep in mind that deformation mechanisms may change profoundly with increasing pressure, as suggested by the change in anisotropy of ferropericlase and magnesium silicate perovskite at high pressure (Karki *et al.*, 1997a, 1997b). The largest uncertainty may be in understanding how polycrystals respond to mantle flow at large finite strains (Blackman *et al.*, 1996; Chastel *et al.*, 1993; Ribe, 1989). This is necessary for estimating the strength of the texture, and the resulting magnitude of anisotropy.

Uncertainties related to composite effects are largest in the context of partial melts. The geometry of the melt phase, whether it exists as spheres, needles, or disks, has an enormous effect on the rock shear elasticity. What is required is an understanding of the relevant mineral–melt interface energetics that control this geometry. Melt geometry may be scale dependent, as demonstrated by experiments in which the melt geometry changes fundamentally on deformation (Bruhn *et al.*, 2000).

1.22.4.3   Implications for Inversions

There are essentially two approaches used for linking seismology and mineral physics, forward and inverse modeling. For the first, a mineralogical model based on an assumed bulk composition, and potential temperature is compared with seismological observations (Duffy and Anderson, 1989; Ita and Stixrude, 1992; Stixrude and Lithgow-Bertelloni, 2005a; Vacher *et al.*, 1998). (For applications to adiabatic temperature profiles in the Earth, the 'potential temperature' refers to the temperature on the adiabat at zero pressure.) In practice, mineralogical models are typically compared with seismological models, an approach that is fraught with difficulty because the seismological models are derivative of the data and nonunique. These difficulties are particularly prevalent in the upper mantle, where lateral variations, attenuation, and anisotropy are all large, and radial models are prone to mislead.

A promising alternative forward modeling approach, little used as yet, would be to compute the actual seismological observables (e.g., traveltimes, mode frequencies, and the like) directly from the mineralogical model. This would permit much more direct and certain comparison to the structure of Earth. The uncertainties inherent in the forward model can in principle be assessed and propagated to uncertainties in predicted seismological observables.

An additional benefit of forward mineralogical models is that they might be used as a reference for seismic tomographic inversions. Tomographic models are usually determined as deviations from an assumed radial structure, and the radial model may bias the inversion. For example, in oceanic regions of the upper mantle, tomographic inversions based on Preliminary Reference Earth Model (PREM) (Dziewonski and Anderson, 1981) might be biased by the large Lehmann discontinuity in this radial model, which subsequent studies have found is preferentially located under continents. PREM and other radial seismic models assume a parametrically simple radial structure. For example, the transition-zone gradient is assumed to be linear, which does not agree with expectations based on the phase transformations that we know take place in typical mantle lithologies. Advantages of using a mineralogical model would be that all anticipated structure from phase transitions would be included. Moreover, the reference state would be one associated with a well-defined, if imprecise physical meaning in terms of bulk composition and geotherm. Recent attempts to construct such so-called 'physical reference models' adjust the mineralogical model to conform with seismological data (Cammarano *et al.*, 2003). By optimizing the fit of the forward model to seismic data, one obtains a more stable starting point for tomographic inversions, but the connection to a physically well-defined reference state is lost. With ever-improving knowledge of mantle phase equlibria and physical properties, one may envision substantial improvements in the construction of mineralogical models and our ability to interpret seismological observations in terms of radial and lateral variations in temperature, and bulk composition.

An inverse model would seek to invert seismic observations directly for radial and lateral variations

in bulk composition and temperature. In practice, inverse models have been based on the intermediate step of a velocity model. Several studies have inverted radial or 3-D velocity and density models for radial and lateral variations in temperature and bulk composition (Deschamps and Trampert, 2003; Goes *et al.*, 2000; Mattern *et al.*, 2005; Shapiro and Ritzwoller, 2004; Stixrude *et al.*, 1992; Trampert *et al.*, 2001). Some caution is in order because of the uncertainty in the nonlinear and linked phenomena involved, particularly in the estimate of attenuation. Also important are systematic effects that have not been included in these inversions. There are three sources of lateral heterogeneity in the mantle, due to lateral variations of temperature, bulk composition, and phase. The last of these has not been included, even though lateral variations in phase proportions can contribute as much to – even more than – 3-D structure as lateral variations in temperature alone. The quantities necessary to estimate the influence of phase on lateral structure are reasonably well known in the upper mantle and transition zone: phase equilibria and physical properties of the minerals involved are experimentally documented, and should be included in future efforts.

1.22.5   Conclusions and Outlook

The contact between mineral physics and seismology of Earth's mantle has grown considerably richer and more sophisticated in recent years. Birch's vision of constraining the chemical and thermal state of the mantle on the basis of mineralogical properties and seismic observations is becoming a reality. In addition, mineral physics is beginning to provide the foundation required for inferring the dynamic state of the mantle, and some aspects of its geological evolution, from the seismological observations.

Progress will come from continued expansion of our knowledge of the elastic properties of mantle minerals at *in situ* conditions of high pressure and high temperature. These data remain the basis for any discussion of mantle structure in terms of radial or lateral variations in temperature or bulk composition. Among recent experimental advances has been a dramatic increase in the pressure range over which measurements of the shear modulus can be made, to 1 Mb (2300 km depth) (Murakami *et al.*, 2006). Coupled with methodological developments for measuring sound velocities at high temperature (Li *et al.*, 2004; Sinogeikin *et al.*, 2004), one may

envision measurement of the elastic properties of mantle minerals at pressure–temperature conditions of the mantle for the first time in the near future. At the same time, first-principles theory continues to make important strides, including the computation of the elastic constants of important phases over the entire mantle pressure–temperature regime (Wentzcovitch *et al.*, 2004).

Equally important will be a better understanding of recently discovered physics and chemistry, including the postperovskite phase transition, the high-spin–low-spin transition of iron in oxides and silicates, and the possible role of valence state changes of iron at high pressure. Among physical properties that are still poorly understood is the attenuation (or its inverse, the quality factor Q). While recent experiments have laid an important foundation (Gribb and Cooper, 1998; Jackson *et al.*, 2002, 2004), we still have little experimental data bearing on the influence of pressure or water content on attenuation. Also uncertain are the dominant deformation mechanisms in mantle minerals at high pressure and temperature, and these provide an additional link between experimental measurements of the elastic-constant tensor and seismically observed anisotropy. Recent experimental discoveries suggest that more surprises await (Mainprice *et al.*, 2005).

Along with improved knowledge of the physical properties of individual phases will come increasing understanding of aggregate properties and the construction of mineralogical models of the mantle as a whole. An important advance will be closer contact between mineralogical models and seismological observations.

References

Abramson EH, Brown JM, and Slutsky LJ (1999) Applications of impulsive stimulated scattering in the earth and planetary sciences. *Annual Review of Physical Chemistry* 50: 279–313.

Agnon A and Bukowinski MST (1990) Delta-S at high-pressure and Dlnvs/Dlnvp in the lower mantle. *Geophysical Research Letters* 17: 1149–1152.

Anderson DL and Given JW (1982) Absorption-band Q model for the Earth. *Journal of Geophysical Research* 87: 3893–3904.

Anderson OL (1995) *Equations of State of Solids for Geophysics and Ceramic Science*. Oxford, UK: Oxford University Press.

Anderson OL and Isaak DG (1995) Elastic constants of mantle minerals at high temperature. In: Ahrens TJ (ed.) *Mineral Physics and Crystallography: A Handbook of Physical Constants*, pp. 64–97. Washington, DC: American Geophysical Union.

Ashcroft NW and Mermin ND (1976) *Solid State Physics*. New York: Holt Rinehart and Winston.

Backus GE (1962) Long-wave elastic anisotropy produced by horizontal layering. *Journal of Geophysical Research* 67: 4427–4440.

Badro J, Fiquet G, Guyot F, *et al.* (2003) Iron partitioning in Earth's mantle: Toward a deep lower mantle discontinuity. *Science* 300: 789–791.

Badro J, Rueff J-P, Vanko G, Monaco G, Fiquet GA, and Guyot F (2004) Electronic transitions in perovskite: Possible nonconvecting layers in the lower mantle. *Science* 305: 383–386.

Barron THK, Berg WT, and Morrison JA (1957) The thermal properties of alkali halide crystals. 2. Analysis of experimental results. *Proceedings of the Royal Society of London Series A, Mathematical and Physical Sciences* 242: 478–492.

Berryman JG (1995) Mixture theories for rock properties. In: Ahrens TJ (ed.) *Rock Physics and Phase Relations: A Handbook of Physical Constants*, pp. 205–228. Washington, DC: American Geophysical Union.

Blackman DK, Kendall JM, Dawson PR, Wenk H-R, Boyce D, and Morgan JP (1996) Teleseismic imaging of subaxial flow at mid-ocean ridges: Traveltime effects of anisotropic mineral texture in the mantle. *Geophysical Journal International* 127: 415–426.

Born M and Huang K (1954) *Dynamical Theory of Crystal Lattices*. Oxford, UK: Clarendon Press.

Bracewell RN (1999) *The Fourier Transform and Its Applications* 3rd edn. New York: McGraw-Hill.

Brown JM and McQueen RG (1986) Phase transitions, Grüneisen parameter, and elasticity for shocked iron between 77 GPa and 400 GPa. *Journal of Geophysical Research* 91: 7485–7494.

Brown JM, Slutsky LJ, Nelson KA, and Cheng L-T (1989) Single-crystal elastic-constants for San Carlos Peridot – An application of impulsive stimulated scattering. *Journal of Geophysical Research-Solid Earth and Planets* 94: 9485–9492.

Bruhn D, Groebner N, and Kohlstedt DL (2000) An interconnected network of core-forming melts produced by shear deformation. *Nature* 403: 883–886.

Bunge HJ, Kiewel R, Reinert T, and Fritsche L (2000) Elastic properties of polycrystals – Influence of texture and stereology. *Journal of The Mechanics and Physics of Solids* 48: 29–66.

Cammarano F, Goes S, Vacher P, and Giardini D (2003) Inferring upper-mantle temperatures from seismic velocities. *Physics of the Earth and Planetary Interiors* 138: 197–222.

Chastel YB, Dawson PR, Wenk H-R, and Bennett K (1993) Anisotropic convection with implications for the upper-mantle. Journal of Geophysical Research, *Solid Earth* 98: 17757–17771.

Chopelas A and Boehler R (1989) Thermal-expansion measurements at very high-pressure, systematics, and a case for a chemically homogeneous mantle. *Geophysical Research Letters* 16: 1347–1350.

Cooper RF (2002) Seismic wave attenuation: Energy dissipation in viscoelastic crystalline solids. In: Karato S and Wenk H-R (eds.) *Plastic Deformation of Minerals and Rocks*, pp. 253–290. Washington, DC: American Mineralogical Society.

Cordier P (2002) Dislocations and slip systems of mantle minerals. In: Karato S and Wenk H-R (eds.) *Plastic Deformation of Minerals and Rocks*, pp. 137–179. Washington, DC: American Mineralogical Society.

Davies GF (1974) Effective elastic-moduli under hydrostatic stress.1. Quasi-harmonic theory. *Journal of Physics and Chemistry of Solids* 35: 1513–1520.

Deschamps F and Trampert J (2003) Mantle tomography and its relation to temperature and composition. *Physics of the Earth and Planetary Interiors* 140: 277–291.

Dove MT (1993) *Introduction to Lattice Dynamics*. Cambridge, UK: Cambridge University Press.

Duffy TS and Ahrens TJ (1992) Sound velocities at high-pressure and temperature and their geophysical implications. *Journal of Geophysical Research-Solid Earth* 97: 4503–4520.

Duffy TS and Anderson DL (1989) Seismic Velocities in Mantle Minerals and the Mineralogy of the Upper Mantle. *Journal of Geophysical Research – Solid Earth and Planets* 94: 1895–1912.

Duffy TS, Zha CS, Downs RT, Mao HK, and Hemley RJ (1995) Elasticity of Forsterite to 16 GPa and the composition of the upper-mantle. *Nature* 378: 170–173.

Dziewonski AM and Anderson DL (1981) Preliminary reference earth model. *Physics of the Earth and Planetary Interiors* 25: 297–356.

Faul UH, Fitz Gerald JD, and Jackson I (2004) Shear wave attenuation and dispersion in melt-bearing olivine polycrystals: 2. Microstructural interpretation and seismological implications. *Journal of Geophysical Research-Solid Earth* 109: N6.

Faul UH and Jackson I (2005) The seismological signature of temperature and grain size variations in the upper mantle. *Earth and Planetary Science Letters* 234: 119–134.

Frankel A and Clayton RW (1986) Finite-difference simulations of seismic scattering – implications for the propagation of short-period seismic-waves in the crust and models of crustal heterogeneity. *Journal of Geophysical Research-Solid Earth and Planets* 91: 6465–6489.

Frost DJ, Liebske C, Langenhorst F, McCammon CA, Trønnes RG, and Rubie DC (2004) Experimental evidence for the existence of iron-rich metal in the Earth's lower mantle. *Nature* 428: 409–412.

Gieske JH and Barsch GR (1968) Pressure dependence of elastic constants of single crystalline aluminum oxide. *Physica Status Solidi* 29: 121–131.

Gillet P, Guyot F, and Wang Y (1996) Microscopic anharmonicity and equation of state of $MgSiO_3$ – Perovskite. *Geophysical Research Letters* 23: 3043–3046.

Goes S, Govers R, and Vacher P (2000) Shallow mantle temperatures under Europe from P and S wave tomography. *Journal of Geophysical Research-Solid Earth* 105: 11153–11169.

Goto TI, Ohno I, and Sumino Y (1976) The determination of the elastic constants of natural almandine-pyrope garnet by rectangular parallelepiped resonance method. *Journal of Physics of the Earth* 24: 149–156.

Gribb TT and Cooper RF (1998) Low-frequency shear attenuation in polycrystalline olivine: Grain boundary diffusion and the physical significance of the Andrade model for viscoelastic rheology. *Journal of Geophysical Research-Solid Earth* 103: 27267–27279.

Hashin Z and Shtrikman S (1962) A variational approach to the theory of the elastic behavior of polycrystals. *Journal of the Mechanics and Physics of Solids* 10: 343–352.

Hashin Z and Shtrikman S (1963) A variational approach to the theory of the elastic behaviour of multiphase materials. *Journal of the Mechanics and Physics of Solids* 11: 127–140.

Hazen RM, Downs RT, and Finger LW (1996) High-pressure crystal chemistry of $LiScSiO_4$: An olivine with nearly isotropic compression. *American Mineralogist* 81: 327–334.

Hedlin MAH, Peter MS, and Paul SE (1997) Seismic evidence for small-scale heterogeneity throughout the Earth's mantle. *Nature* 387: 145–150.

Heinz D, Jeanloz R, and O'Connell RJ (1982) Bulk attenuation in a polycrystalline earth. *Journal of Geophysical Research* 87: 7772–7778.

Helbig K (1984) *Foundations of Anisotropy for Exploration Seismics*. New York: Pergamon.

Hill R (1952) The elastic behaviour of a crystalline aggregate. *Proceedings of the Physical Society of London Section A* 65: 349–355.

Hill R (1963) Elastic properties of reinforced solids – Some theoretical principles. *Journal of the Mechanics and Physics of Solids* 11: 357–372.

Holland TJB and Powell R (1998) An internally consistent thermodynamic data set for phases of petrological interest. *Journal of Metamorphic Geology* 16: 309–343.

Isaak DG, Anderson OL, and Cohen RE (1992) The relationship between shear and compressional velocities at high pressures: Reconciliation of seismic tomography and mineral physics. *Geophysical Research Letters* 19: 741–744.

Isaak DG, Cohen RE, and Mehl MJ (1990) Calculated elastic constants and thermal properties of MgO at high pressures and temperatures. *Journal of Geophysical Research* 95: 7055–7067.

Ita J and Stixrude L (1992) Petrology, elasticity, and composition of the mantle transition zone. *Journal of Geophysical Research-Solid Earth* 97: 6849–6866.

Jackson DD and Anderson DL (1970) Physical mechanisms of seismic-wave attenuation. *Reviews of Geophysics and Space Physics* 8: 1.

Jackson I (2000) Geophysics – Taking the earth's temperature. *Nature* 406: 470–471.

Jackson I, Faul UH, Fitz Gerald JD, John D, and Tan BH (2004) Shear wave attenuation and dispersion in melt-bearing olivine polycrystals: 1. Specimen fabrication and mechanical testing. *Journal of Geophysical Research-Solid Earth* 109: N(6).

Jackson I, Fitz Gerald JD, Faul UH, and Tan BH (2002) Grain-size-sensitive seismic wave attenuation in polycrystalline olivine. *Journal of Geophysical Research-Solid Earth* 107: N12.

Jackson I and Niesler H (1982) The elasticity of periclase to 3 GPa and some geophysical implications. In: Akimoto S and Manghnani MH (eds.) *High-pressure Research in Geophysics*, pp. 93–133. Tokyo, Japan: Center for Academic Publications.

Jackson JM, Sinogeikin SV, and Bass JD (2000) Sound velocities and elastic properties of gamma-Mg_2SiO_4 to 873 K by Brillouin spectroscopy. *American Mineralogist* 85: 296–303.

Jeanloz R and Thompson (1983) Phase transitions and mantle discontinuities. *Reviews of Geophysics* 21: 51–74.

Jiang FM, Speziale S, and Duffy TS (2004) Single-crystal elasticity of grossular – and almandine-rich garnets to 11 GPa by Brillouin scattering. *Journal of Geophysical Research-Solid Earth* 109: N10.

Juanzemis W (1967) *Continuum Mechanics*. New York: MacMillan.

Karato S (1993) Importance of anelasticity in the interpretation of seismic tomography. *Geophysics Research Letters* 20: 1623–1626.

Karato S-I (1998) Seismic anisotropy in the deep mantle, boundary layers and the geometry of mantle convection. *Pure and Applied Geophysics* 151: 565–587.

Karki BB and Crain J (1998) First-principles determination of elastic properties of $CaSiO_3$ perovskite at lower mantle pressures. *Geophysical Research Letters* 25: 2741–2744.

Karki BB, Stixrude L, Clark SJ, Warren MC, Ackland GJ, and Crain J (1997a) Elastic Properties of orthorhombic $MgSiO_3$ perovskite at lower mantle pressures. *American Mineralogist* 82: 635–638.

Karki BB, Stixrude L, Clark SJ, Warren MC, Ackland GJ, and Crain J (1997b) Structure and elasticity of MgO at high pressure. *American Mineralogist* 82: 51–60.

Karki BB, Karki BB, Stixrude L, and Wentzcovitch RM (2001) High-pressure elastic properties of major materials of Earth's mantle from first principles. *Reviews of Geophysics* 39: 507–534.

Kennett BLN and Engdahl ER (1991) Traveltimes for global earthquake location and phase identification. *Geophysical Journal International* 105: 429–465.

Kiefer B, Stixrude L, and Wentzcovitch RM (1997) Elastic constants and anisotropy of Mg_2SiO_4 spinel at high pressure. *Geophysical Research Letters* 24: 2841–2844.

Kieffer SW (1979) Thermodyanamics and lattice vibrations of minerals, I: mineral heat capacities and their relationship to simple lattice vibrational modes. *Reviews of Geophysics and Space Physics* 17: 1–19.

Kieffer SW (1980) Thermodynamics and lattice-vibrations of minerals 4. Application to chain and sheet silicates and orthosilicates. *Reviews of Geophysics* 18: 862–886.

Kosevich AM, Lifshitz EM, Landau LD, and Pitaevskii LP (1986) *Theory of Elasticity* 3rd edn. 195 pp. Oxford, UK: Butterworth-Heinemann.

Li BS, Kung J, and Liebermann RC (2004) Modern techniques in measuring elasticity of Earth materials at high pressure and high temperature using ultrasonic interferometry in conjunction with synchrotron x-radiation in multi-anvil apparatus. *Physics of the Earth and Planetary Interiors* 143: 559–574.

Lin JF, Struzhkin VV, Jacobsen SD, *et al.* (2005) Spin transition of iron in magnesiowustite in the Earth's lower mantle. *Nature* 436: 377–380.

Liu J, Chen G, Gwanmesia GD, and Liebermann RC (2000) Elastic wave velocities of pyrope-majorite garnets (Py(62)Mj(38) and Py(50)Mj(50)) to 9 GPa. *Physics of the Earth and Planetary Interiors* 120: 153–163.

Mainprice D, Andréa T, Hélène C, Patrick C, and Daniel JF (2005) Pressure sensitivity of olivine slip systems and seismic anisotropy of Earth's upper mantle. *Nature* 433: 731–733.

Mattern E, Matas J, Ricard Y, and Bass J (2005) Lower mantle composition and temperature from mineral physics and thermodynamic modelling. *Geophysical Journal International* 160: 973–990.

Mcqueen RG, Marsh SP, Taylor JW, Fritz JN, and Carter WJ (1970) The equation of state of solids from shock wave studies. In: Kinslow R (ed.) *High-velocity Impact Phenomena*, pp. 293–417. New York, NY: Academic Press.

Mei S and Kohlstedt DL (2000a) Influence of water on plastic deformation of olivine aggregates 1. Diffusion creep regime. *Journal of Geophysical Research-Solid Earth* 105: 21457–21469.

Mei S and Kohlstedt DL (2000b) Influence of water on plastic deformation of olivine aggregates 2. Dislocation creep regime. *Journal of Geophysical Research – Solid Earth* 105: 21471–21481.

Merkel S, Goncharov AF, Mao HK, Gillet P, and Hemley RJ (2000) Raman spectroscopy of iron to 152 gigapascals: Implications for Earth's inner core. *Science* 288: 1626–1629.

Murakami M, Sinogeikin SU, Hellwig H, Bass JD, and Li J (2006) Sound velocity of $MgSiO_3$ perovskite to Mbar pressure. *Earth and Planetary Science Letters* 256: 47–54.

Nowick AS and Berry BS (1972) *Anelastic Relaxation in Crystalline Solids*. New York and London: Academic Press.

Nye JF (1985) *Physical Properties of Crystals: Their Representation by Tensors and Matrices,* 2 edn. Oxford, UK: Oxford University Press.

Oganov AR, Gillan MJ, and Price GD (2003) *Ab initio* lattice dynamics and structural stability of MgO. *Journal of Chemical Physics* 118: 10174–10182.

Pasternak MP, Taylor RD, Jeanloz R, Li X, Nguyen JH, and Mccammon CA (1997) High pressure collapse of magnetism in Fe0.94O: Mossbauer spectroscopy beyond 100 GPa. *Physical Review Letters* 79: 5046–5049.

Ribe NM (1989) Seismic Anisotropy and Mantle Flow. *Journal of Geophysical Research-Solid Earth and Planets* 94: 4213–4223.

Rigden SM, Jackson INS, Niesler H, Liebermann RC, and Ringwood AE (1991) Spinel elasticity and seismic structure of the transition zone of the mantle. *Nature* 354: 143–145.

Rivers ML and Carmichael ISE (1987) Ultrasonic studies of silicate melts. *Journal of Geophysical Research – Solid Earth and Planets* 92: 9247–9270.

Robie RA and Hemingway BS (1995) *Thermodynamic Properties of Minerals and Related Substances at 298.15 K and 1 Bar (10^5 Pascals) Pressure and at Higher Temperature*, 461 pp. Washington, DC: US Geological Survey.

Shapiro NM and Ritzwoller MH (2004) Thermodynamic constraints on seismic inversions. *Geophysical Journal International* 157: 1175–1188.

Shim SH, Jeanloz R, and Duffy TS (2002) Tetragonal structure of $CaSiO_3$ perovskite above 20 GPa. *Geophysical Research Letters* 29: 1399.

Sinogeikin SV and Bass JD (2000) Single-crystal elasticity of pyrope and MgO to 20 GPa by Brillouin scattering in the diamond cell. *Physics of the Earth and Planetary Interiors* 120: 43–62.

Sinogeikin SV and Bass JD (2002) Elasticity of Majorite and a Majorite-Pyrope solid solution to high pressure: Implications for the transition zone. *Geophysical Research Letters* 29(2): 1017 (doi:10.1029/2001GL013937).

Sinogeikin SV, Lakshtanov DL, Nicholas JD, and Bass JD (2004) Sound velocity measurements on laser-heated MgO and Al_2O_3. *Physics of the Earth and Planetary Interiors* 143: 575–586.

Spetzler H (1970) Equation of state of polycrystalline and single-crystal Mgo to 8 kilobars and 800 degrees K. *Journal of Geophysical Research* 75: 2073–2087.

Speziale S, Jiang SF, and Duffy TS (2005a) Compositional dependence of the elastic wave velocities of mantle minerals: Implications for seismic properties of mantle rocks. In: Vander Hilst, Bass JD, Matas J, and Trampert J (eds.) *Earth's Deep Mantle: Structure, Composition, and Evolution*, pp. 301–320. Washington, DC: American Geophysical Union.

Speziale S, Milner A, Lee VE, Clark SM, Pasternak MP, and Jeanloz R (2005b) Iron spin transition in Earth's mantle. *Proceedings of the National Academy of Sciences of the United States of America* 102: 17918–17922.

Speziale S, Zha C-S, Duffy TS, Hemley RJ, and Mao H-K (2001) Quasi-hydrostatic compression of magnesium oxide to 52 GPa: Implications for the pressure-volume-temperature equation of state. *Journal of Geophysical Research-Solid Earth* 106: 515–528.

Stixrude L (1998) Elastic constants and anisotropy of $MgSiO_3$ perovskite, periclase, and SiO_2 at high pressure. In: Gurnis M, Wysession M, Knittle E, and Buffet B (eds.) *The Core–Mantle Boundary Region*, pp. 83–96. Washington, DC: American Geophysical Union.

Stixrude L, Cohen RE, and Singh DJ (1994) Iron at high pressure: Linearized augmented plane wave calculations in the generalized gradient approximation. *Physical Review B* 50: 6442–6445.

Stixrude L, Cohen RE, Yu R, and Krakauer H (1996) Prediction of phase transition in $CaSiO_3$ perovskite and implications for lower mantle structure. *American Mineralogist* 81: 1293–1296.

Stixrude L, Hemley RJ, Fei Y, and Mao HK (1992) Thermoelasticity of silicate perovskite and magnesiowustite and stratification of the earth's mantle. *Science* 257: 1099–1101.

Stixrude L and Lithgow-Bertelloni C (2005a) Mineralogy and elasticity of the oceanic upper mantle: Origin of the low-velocity zone. *Journal of Geophysical Research-Solid Earth* 110: B03204 (doi:10.1029/2004JB002965).

Stixrude L and Lithgow-Bertelloni C (2005b) Thermodynamics of mantle minerals – I. Physical properties. *Geophysical Journal International* 162: 610–632.

Stixrude L, Lithgow-Bertelloni C, Kieter B, and Fumagaelli P (2007) Phase stability and shear softening in $CaSiO_3$ perovskite at high pressure. *Physical Review B* 75: 024108.

Trampert J, Vacher P, and Vlaar N (2001) Sensitivities of seismic velocities to temperature, pressure and composition in the lower mantle. *Physics of the Earth and Planetary Interiors* 124: 255–267.

Vacher P, Mocquet A, and Sotin C (1998) Computation of seismic profiles from mineral physics: The importance of the non-olivine components for explaining the 660 km depth discontinuity. *Physics of the Earth and Planetary Interiors* 106: 275–298.

Wallace DC (1972) *Thermodynamics of Crystals,* 1st edn. New York: Wiley.

Watt JP (1988) Elastic properties of polycrystalline minerals – Comparison of theory and experiment. *Physics and Chemistry of Minerals* 15: 579–587.

Watt JP, Davies GF, and O'Connell RJ (1976) The elastic properties of composite materials. *Reviews of Geophysics and Space Physics* 14: 541–563.

Weidner DJ, Bass J, Ringwood AE, and Sinclair W (1982) The single-crystal elastic moduli of stishovite. *Journal of Geophysical Research* 87: 4740–4746.

Weiner JH (1983) *Statistical Mechanics of Elasticity*, 439 pp. New York: Wiley.

Wentzcovitch RM, Karki BB, Cococcioni M, and Gironcoli S de (2004) Thermoelastic properties of $MgSiO_3$-perovskite: Insights on the nature of the Earth's lower mantle. *Physical Review Letters* 92(1): 018501.

Wentzcovitch RM and Stixrude L (1997) Crystal chemistry of forsterite: A first principles study. *American Mineralogist* 82: 663–671.

Williams Q (1995) Infrared, Raman and optical spectroscopy of earth materials. In: *Mineral Physics and Crystallography*, Ahrens TJ (ed.) *A Handbook of Physical Constants*. Washington, DC: American Geophysical Union.

Williams Q and Garnero EJ (1996) Seismic evidence for partial melt at the base of Earth's mantle. *Science* 273: 1528.

Workman RK and Hart SR (2005) Major and trace element composition of the depleted MORB mantle (DMM). *Earth and Planetary Science Letters* 231: 53–72.

Yoneda A (1990) Pressure derivatives of elastic-constants of single-crystal MgO and $MgAl_2O_4$. *Journal of Physics of the Earth* 38: 19–55.

Zaug JM, Abramson EH, Brown JM, and Slutsky LJ (1993) Sound velocities in olivine at Earth mantle pressures. *Science* 260: 1487–1489.